

Emergent behaviour and phase transitions in spatially distributed multi-cellular metabolic networks

K. Narayanankutty,^{1,2} J. A. Pereiro-Morejón,^{3,4} A. Ferrero,^{1,2} V. Onesto,⁵ S. Forciniti,⁵
L. L. del Mercato,⁵ R. Mulet,^{3,6} A. De Martino,^{7,8,*} D. S. Tourigny,^{9,†} and D. De Martino^{1,10,‡}

¹*Biofisika Institute (CSIC, UPV/EHU), Barrio Sarriena s/n, 48940 Leioa, Bizkaia, Spain*

²*Department of Molecular Biology and Biochemistry, University of the Basque Country, Leioa, Spain*

³*Group of Complex Systems and Statistical Physics, Physics Faculty,*

University of Havana, San Lazaro y L, Vedado, La Habana 10400, Cuba

⁴*Biology Faculty, University of Havana, San Lazaro y L, Vedado, La Habana 10400, Cuba*

⁵*Institute of Nanotechnology, National Research Council (CNR-NANOTEC),
c/o Campus Ecotekne, via Monteroni, 73100 Lecce, Italy*

⁶*Department of Theoretical Physics, University of Havana, San Lazaro y L, Vedado, La Habana 10400, Cuba*

⁷*Politecnico di Torino, Corso Duca degli Abruzzi 24, 10129 Torino, Italy*

⁸*Italian Institute for Genomic Medicine, c/o IRCCS, SP142 km 3,95, 10060 Candiolo, Italy*

⁹*School of Mathematics, University of Birmingham, Edgbaston, B15 2TT, UK*

¹⁰*Ikerbasque Foundation, Bilbao, Spain*

Overflow metabolism is a ubiquitous phenomenon whereby cells in aerobic conditions excrete byproducts of glycolysis, such as lactate or acetate, into the medium in a seemingly wasteful and polluting fashion. Whilst overflow may confer microbes a fitness advantage by allowing them to overcome a finite oxidative capacity, its occurrence in higher organisms is harder to assess. Important insight was however obtained in recent experiments conducted at single-cell resolution, which revealed that accumulation of overflow products in tumor cell cultures known as the ‘Warburg effect’ arises from imbalances in the dynamic and heterogeneous inter-cellular exchange network through which cells collectively regulate the microenvironment. Here we provide a quantitative characterization of this scenario by integrating metabolic network modeling with diffusion constraints, statistical physics theory and single-cell experimental flux data. On the theoretical side, we clarify how diffusion-limited exchanges shape the space of viable metabolic states of a multi-cellular system. Specifically, a phase transition from a balanced network of exchanges to an unbalanced overflow regime occurs as the mean cellular glucose and oxygen uptakes vary while single-cell metabolic phenotypes are highly heterogeneous around this transition. We then show that time-resolved data from human tumor-stroma cell co-cultures consistently map to this crossover region, supporting the idea that environmental deterioration reflects a failure of coordination among recurrently interacting cells. In summary, our findings suggest that, rather than deriving from multiple independent cell-autonomous processes, environmental control is an emergent feature of multi-cellular systems.

Cell populations adapt to an environment on at least two different levels: (i) via intra-cellular regulation (e.g. metabolic, signaling, genetic), which underlies essential maintenance, biosynthetic and, possibly replicative processes; and (ii) via extra-cellular mechanisms (e.g. sensing, signaling, motility), necessary to harvest information and control exchanges with the medium. The latter level prompts inter-cellular interactions and introduces an ecological dimension to multi-cellular systems, where cells can be seen as agents that need to meet certain requirements while jointly modulating a shared environment. The way in which the two layers integrate is a key determinant of adaptation, viability, and ultimately fitness [1–4]. This raises a rather basic question: is a viable environment the result of the straightforward aggregation of a large number of autonomous actions by individual cells, or is it rather an emergent property of the collective behavior of many interacting cells? [5]

The contours of this problem become especially clear upon focusing on a cellular process that directly links the two levels described above, namely carbon overflow (CO). In short, CO consists of the excretion into the medium of carbon-based waste products of intra-cellular carbon catabolism, such as acetate, ethanol, or lactate in aerobic conditions [6, 7]. This may occur when the cell’s oxidative capacity is saturated (e.g. due to excess glucose availability or dysregulated import pathways), so that, even in the presence of abundant oxygen, incoming carbon is diverted towards fermentation [8–11]. CO appears to be a ‘universal’ feature of cellular metabolism, which has been consistently observed across domains. While in microbial systems it can be partly explained by the evolutionary advantage of a higher growth rate at the cost of lower energy yield [12–15], the root cause of CO in higher organisms or in tumors (where it underlies the Warburg effect [16]) is more difficult to ascribe, especially when it is not associated with growth and replication [4, 17–21].

An ecological role for CO derives from the fact that accumulation of fermentation byproducts in the extra-cellular medium leads to acidification and, in turn, detrimental effects ranging from the slowdown of protein

* andrea.demartino@polito.it

† d.tourigny@bham.ac.uk

‡ daniele.demartino@ehu.eus

synthesis to growth inhibition due to apoptosis [22]. Remediation of the shared environment is therefore of paramount importance for cell populations. On the other hand, exporters of overflow products effectively supply the medium with additional carbon equivalents on which cells can rely for sustenance (via oxidation) [23, 24]. Importers thereby contribute to correcting environmental pollution. Taken together, these processes are major drivers of functionally- and ecologically-significant inter-cellular crosstalk [25–28]. Nevertheless, how decisive such a crosstalk is compared to individual cellular decisions in engineering the environment remains an open question.

We attempt to address this issue by integrating (a) constraint-based metabolic modeling (CBM) [29] and diffusion constraints, (b) the statistical physics approach to the study of emergent and collective phenomena [30], and (c) high-resolution data for single-cell behavior in a cell population adapting to a glucose-based medium [31]. More specifically, we first employ CBM to demonstrate that a spatially distributed population of cells with identical metabolic requirements coupled through an exchange network undergoes a crossover between two distinct metabolic regimes when the population-averaged metabolic rate changes. The first regime is characterized by weak medium acidification, while significant accumulation of overflow products occurs in the second. Next, we rationalize these findings mathematically using an analytically tractable approximation of the model. Within this approach, the crossover takes the form of an order-disorder transition similar to those that characterize thermodynamic systems in statistical physics [30], and bulk overflow appears as an emergent feature of a population of interacting cells. Finally, exploiting statistical inference techniques, we show that an experimentally-studied mixed population of cancer cells and cancer-associated fibroblasts self-organizes its collective metabolism over time so that it remains close to the theoretical critical line separating the two regimes, i.e. at the onset of acidification where metabolic heterogeneity is large.

RESULTS

Single-cell metabolic model and flux space

To build our theoretical setup, we begin by modeling the metabolic flux space available to a single mammalian cell through CBM with the minimal reaction network for energy production by central carbon pathways displayed in Fig. 1A. We want to model a typical overflow scenario like the one presented in [31], where the medium is glucose enriched, there is lactate accumulation in aerobic conditions and metabolism is running mainly for the sake of energy production with negligible biomass build-up. At steady state, the equation for carbon mass-balance is

$$u_G + \frac{u_L}{2} - \frac{u_O}{6} = 0 \quad , \quad (1)$$

where $u_G \geq 0$ is the flux for import of glucose from the environment (in units $\text{mmol g}^{-1} \text{h}^{-1}$), u_L is the corresponding lactate exchange flux ($u_L > 0$ for import, $u_L < 0$ for export) and $u_O \geq 0$ is the flux for import of molecular oxygen (that we assume corresponds to respiratory flux, so that it enters the carbon mass-balance due to its equivalence to carbon dioxide secretion). The net rate of ATP production is given by

$$f_{\text{ATP}} = -u_L + 5u_O \quad , \quad (2)$$

where we used empirical coefficients for ATP produced by respiration and fermentation pathways (Supporting Information, Sec. S1). Along with (1), the space of viable fluxes is defined by the additional constraints

$$0 \leq u_G \leq U_G \quad (3)$$

$$0 \leq u_O \leq U_O \quad (4)$$

$$f_{\text{ATP}} \geq L_M \quad (5)$$

representing respectively the limited capacities of glucose import channels (Eq. (3)) and mitochondrial activity (Eq. (4)), and a minimal rate of energy production required for cell maintenance (Eq. (5)). Values for the parameters U_G , U_O and L_M are also available from the literature (Supporting Information, Sec. S1).

The resulting single-cell flux space is represented by the 2-dimensional polytope in the (u_O, u_G) plane shown in Fig. 1B, whose oblique boundary corresponds to the maintenance requirement (5). Lactate fluxes can be read off from (1). The line separating the purple and pink shaded regions corresponds to states with $u_L = 0$. States with constant but non-zero lactate exchange are represented by lines parallel to it. In particular, states with $u_L > 0$ (resp. $u_L < 0$), i.e. with lactate import (resp. export) foliate the purple (resp. pink) shaded region. In the absence of environmental lactate, an isolated cell can only attain states with $u_L \leq 0$ (no lactate import). In the presence of a lactate source, however, states with $u_L > 0$ (lactate import) become accessible. We shall use the symbol \mathcal{F}_1 to denote the viable single-cell flux space of Fig. 1B. An independent cell that autonomously adjusts its metabolism to optimize a linear objective function (as in Flux Balance Analysis [32]) would be found at specific points on the boundary of \mathcal{F}_1 . For instance (Fig. 1B), at point A if it maximises the rate of ATP production. (More examples are given in the caption of Fig. 1.)

Exchange coupling and multi-cellular flux space

When N cells share the same extra-cellular environment, lactate-excreting cells effectively act as lactate sources. This makes the $u_L > 0$ portion of \mathcal{F}_1 potentially accessible to other cells (purple region in Fig. 1B) even if there is no external source of lactate in the culture. Cells therefore become metabolically coupled through the exchange of lactate, as endogenous lactate gets shuttled

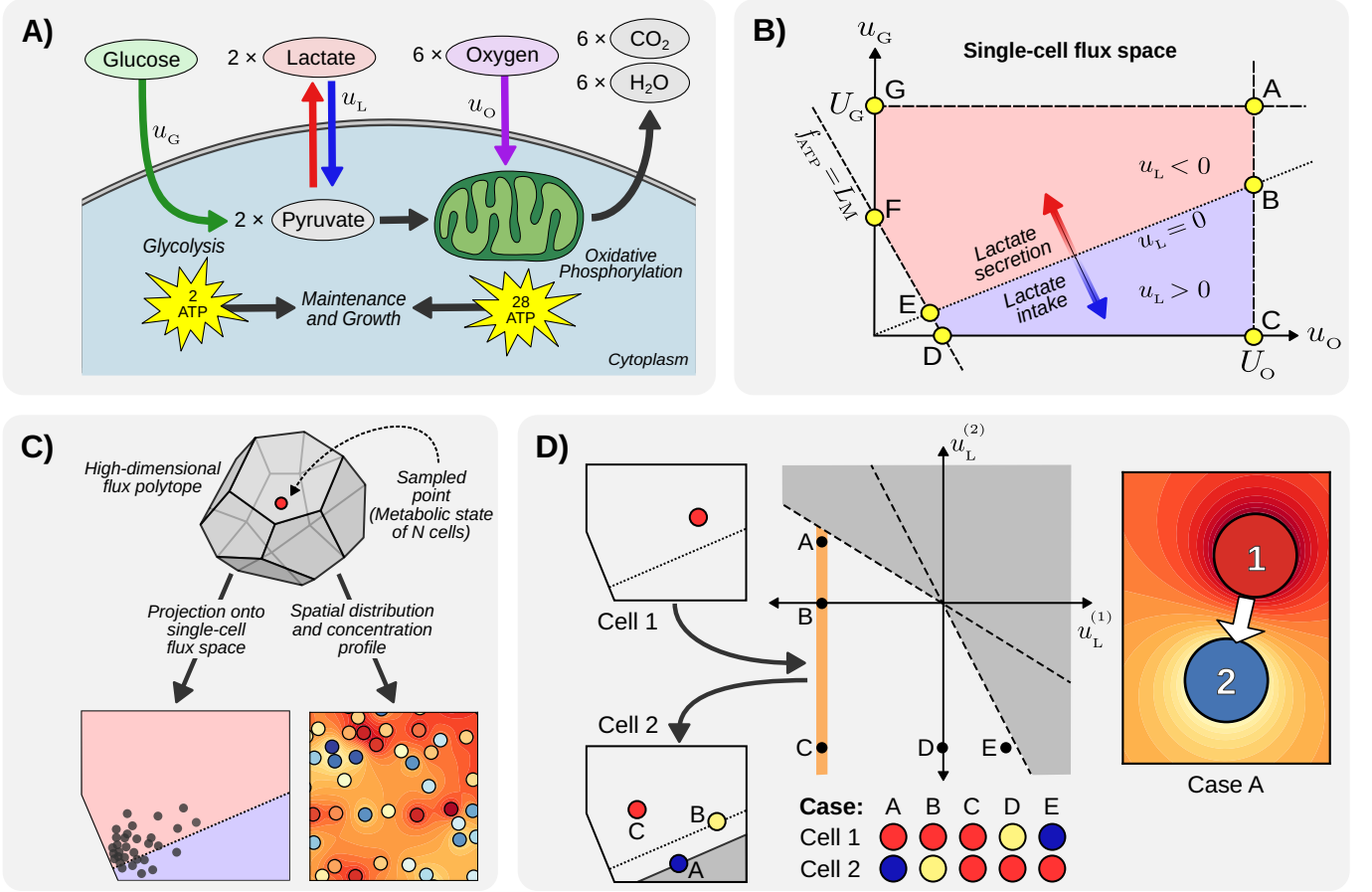


FIG. 1: Constraint-based metabolic model. (A) Sketch of the single-cell metabolic network representing the central carbon pathways (u_G glucose uptake, u_L lactate flux, u_O oxygen uptake). (B) Feasible single-cell flux space (\mathcal{F}_1) in the (u_O, u_G) plane, bounded by Eqs (3) (glucose intake), (4) (oxygen intake), and (5) (ATP maintenance). For a single cell (as well as for the average bulk behaviour) the purple region ($u_L > 0$ or lactate import) is unfeasible unless lactate is exogenously provided. Points A-G are those where the cell would maximise rate of ATP production (A), maximise rate of ATP production with zero net lactate exchange (B), maximise rate of ATP production while using lactate as the only carbon source (C), minimise rate of ATP production while using lactate as the only carbon source (D), minimise rate of ATP production with zero net lactate exchange (E), minimise rate of ATP production anaerobically (F), or maximise rate of lactate excretion (G). (C) The possibility for cells to exchange lactate defines an extended metabolic flux space for a system of N cells (\mathcal{F}_N) whose configurations can be projected into single-cell flux space. In turn, the corresponding lactate fluxes define a spatial concentration gradient in the medium via (8). (D) Case $N = 2$, feasible space in the plane $(u_L^{(1)}, u_L^{(2)})$. In cases A and E cells are coupled via lactate exchange, one cell acting as a donor (red) for the other (blue). This makes the $u_L > 0$ (purple) region of panel (B) viable for the acceptor cell even in absence of an external lactate source.

across the population by diffusion. By modeling cells as spherical sources or sinks of lactate, with radius R and located at fixed positions \mathbf{r}_i ($i = 1, 2, \dots, N$), one can show that, at steady state, the lactate exchange fluxes $u_L^{(i)}$ of all cells must obey an additional set of N constraints described by (Supporting Information, Sec. S2; see also [33])

$$\sum_{j=1}^N A_{ij} u_L^{(j)} \leq 0 \quad (i = 1, 2, \dots, N), \quad (6)$$

$$A_{ij} = \delta_{ij} + (1 - \delta_{ij}) \frac{R}{|\mathbf{r}_i - \mathbf{r}_j|} > 0, \quad (7)$$

where $|\mathbf{r}_i - \mathbf{r}_j| \geq 2R$ and $\delta_{ij} = 1$ if $i = j$ and zero otherwise. Combined with N copies of constraints (1) and (3)-(5), one for each cell i , the inequalities (6) define a $2N$ -dimensional convex polytope containing the feasible flux configurations of a system of N cells coupled through diffusion-limited lactate exchanges (Fig. 1C). We henceforth denote this total space by \mathcal{F}_N . In turn, each point in \mathcal{F}_N can be represented by N points in the single-cell space \mathcal{F}_1 (one per cell, Fig. 1C). It is finally possible to reconstruct the spatial concentration profile of lactate by assuming that lactate levels in the culture obey the Laplace equation. Specifically, the concentration at po-

sition \mathbf{r} is given by (Supporting Information, Sec. S2)

$$c_L(\mathbf{r}) = \sum_{i=1}^N \frac{u_L^{(i)}}{D_L |\mathbf{r} - \mathbf{r}_i|} + B(\mathbf{r}) \quad , \quad (8)$$

where D_L is the diffusion constant of lactate and $B(\mathbf{r})$ is a term accounting for exchanges with the boundary of the system. (Note that we are assuming that cells are identical, in that the parameters U_G, U_O, L_M and R are the same for each cell, and that there is no competition for nutrients other than lactate.)

The effect of the diffusion constraint is most easily visualized diagrammatically in the case of two cells ($N = 2$, Fig. 1D), where the maximal lactate uptake rate for one cell is determined by both a minimum rate of lactate production by the other and the distance between them (reflected in the slopes of the dashed lines in Fig. 1D). Clearly, (6) does not allow for both cells to import lactate ($u_L^{(1)} > 0, u_L^{(2)} > 0$) if none is being supplied externally. This picture generalizes to N cells: it can be shown (Supporting Information, Sec. S3) that environmental lactate accumulation ($\sum_{i=1}^N u_L^{(i)}$) can not be zero unless the lactate flux of each individual cell vanishes. Conversely, if lactate is exchanged between any cells within the population then there must be some non-zero leakage of lactate in the medium, i.e. an accumulation of overflow product akin to the Warburg effect.

Environmental lactate spillover as a failure of inter-cellular coordination

While constraints (1) and (3)-(6) define the space \mathcal{F}_N of feasible, multi-cellular metabolic flux configurations and implicitly include a lactate exchange network, an interpretation in terms of population-level metabolic states is not straightforward. To get a deeper understanding, we resorted to a statistical approach based on sampling \mathcal{F}_N according to a controllable probabilistic rule. A simple and theoretically convenient choice for a probability density over the $2N$ -dimensional flux space is given by the Boltzmann distribution [34]

$$p(\mathbf{u}|\beta) = \frac{\exp[\beta h(\mathbf{u})]}{Z(\beta)} \quad (\mathbf{u} \in \mathcal{F}_N) \quad , \quad (9)$$

where $\mathbf{u} \equiv \{(u_G^{(i)}, u_O^{(i)})\}_{i=1}^N$ denotes an N -cell configuration of metabolic degrees of freedom, β is a numerical parameter, h is a prescribed function of the glucose and oxygen import fluxes of every cell, while

$$Z(\beta) = \int_{\mathcal{F}_N} \exp[\beta h(\mathbf{u})] d\mathbf{u} \quad (10)$$

is a factor ensuring normalization over \mathcal{F}_N . For $\beta = 0$, (9) coincides with the uniform distribution over \mathcal{F}_N , under which each viable N -cell state is equally likely. When

$\beta \rightarrow +\infty$ (resp. $\beta \rightarrow -\infty$), instead, the sampling concentrates on N -cell states of maximum (resp. minimum) h . Notably, since:

$$\langle h \rangle_\beta \equiv \frac{1}{N} \int_{\mathcal{F}_N} h(\mathbf{u}) p(\mathbf{u}|\beta) d\mathbf{u} = \frac{\partial}{\partial \beta} \ln Z(\beta) \quad , \quad (11)$$

$$\sigma_h^2 \equiv \langle h^2 \rangle_\beta - \langle h \rangle_\beta^2 = \frac{\partial^2}{\partial \beta^2} \ln Z(\beta) \quad (12)$$

fixing the value of β is equivalent to constraining the population-averaged value of h while still allowing for variability in single-cell metabolic profiles. Most importantly, for any β , (9) describes the distribution with constrained mean value of h having *maximum entropy*, and thus being the least unbiased [34]. As β changes, therefore, (9) allows the exploration of a broad range of population-level features.

In our specific case, the overall glucose and oxygen import fluxes represent natural choices for h . To gain additional sampling freedom, we therefore opted for a version of (9) that allows to maximise or minimise these quantities independently, i.e. ($\mathbf{u} \in \mathcal{F}_N$)

$$p(\mathbf{u}|\beta_G, \beta_O) \propto \exp \left[\beta_G \sum_{i=1}^N u_G^{(i)} + \beta_O \sum_{i=1}^N u_O^{(i)} \right] \quad , \quad (13)$$

where β_G and β_O are real parameters. (Identities similar to (11) and (12) valid for (13) are given in Supporting Information, Sec. S4). We then sampled \mathcal{F}_N according to (13) for different values of β_G and β_O via Hit-and-Run Monte Carlo (Supporting Information, Sec. S5, and [35]). Key representative configurations for 150 cells uniformly scattered at random [36] over an area of 0.5×0.5 mm² are showcased in Fig. 2A.

We focus our attention on the case where β_O is fixed to a finite value and β_G is varied from $-\infty$ to $+\infty$ (Fig. 2A and B), thereby modulating the mean glucose consumption in the population. When $\beta_G \rightarrow -\infty$, cells independently maximise their ATP/glucose yields (Fig. 2A, leftmost panel), corresponding to point E in Fig. 1B. With our (biologically plausible) choice of parameters, this leads to a homogeneous configuration where all cells run on respiration, none produce lactate, and thus no lactate accumulates in the medium (Fig. 2B, leftmost panel). As β_G increases, cells begin to excrete and import lactate, leading to highly heterogeneous lactate fluxes. Remarkably, the resulting spillover is very small, implying that the lactate exchange network is nearly balanced in spite of the presence of large excretion fluxes. However, a further increase in β_G destabilizes the network, causing lactate to accumulate in the medium at significant levels (Fig. 2A and B, middle panels). Finally, for $\beta_G \rightarrow +\infty$, when cells independently maximise their ATP production rates (Fig. 2A, rightmost panel), the population returns to a homogeneous state in which all cells run strongly on fermentation and excrete large amounts of lactate (Fig. 2B, rightmost panel). This corresponds to point A in Fig. 1B.

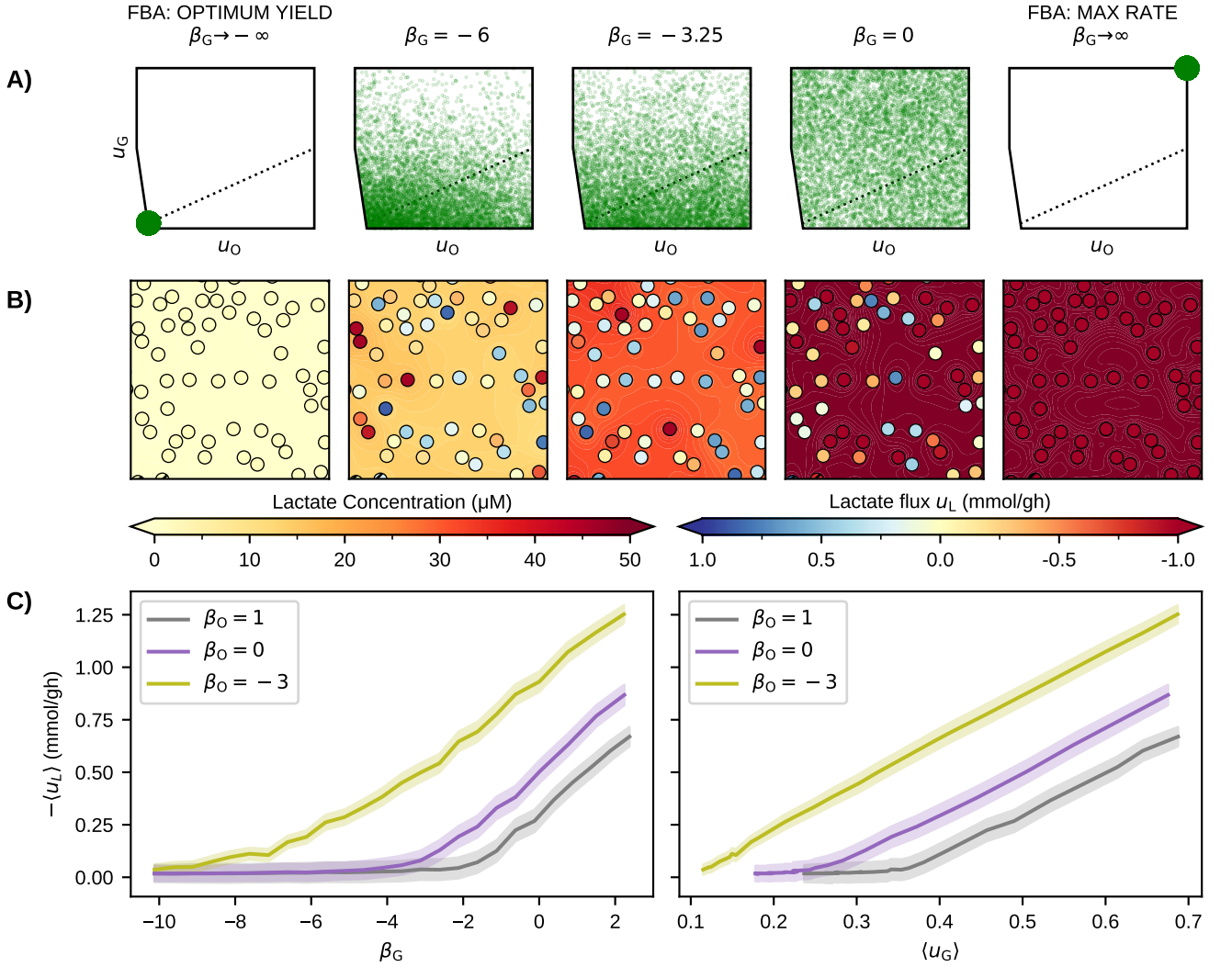


FIG. 2: Emergent bulk overflow in CBM simulations. Simulations are performed by sampling the feasible space \mathcal{F}_N for $N = 150$ cells distributed over an area of $500 \times 500 \mu\text{m}^2$ according to (13) via Hit-and-Run Monte Carlo Markov chains for fixed $\beta_O = 0$ and different values of β_G . This interpolates between the states of maximum ATP yield ($\beta_G \rightarrow -\infty$) and maximum ATP rate ($\beta_G \rightarrow \infty$). (A) Multi-cellular flux configurations projected into single-cell space in the (u_O, u_G) plane (same as in Fig. 1B) for different values of β_G . (B) Typical spatial lactate concentration gradient across the culture (background color) and single cell lactate fluxes (circles color) for the same values of β_G as in Panel A. (C) Average net lactate excretion fluxes ($-\langle u_L \rangle$) as a function of β_G (left) and of the average glucose uptake (right) for different values of β_O . Notice the approximately threshold-linear behaviour for larger values of β_O .

The crossover from the state of maximum ATP yield to the state of maximum ATP rate is clearly reflected by the fact that the averaged net flux of lactate excretion across the population ($-\langle u_L \rangle$) increases as β_G increases (Fig. 2C). We observe that a range of values of β_O exists for which $-\langle u_L \rangle$ closely resembles a threshold-linear function of β_G , marking a sharp transition between regimes with small and large lactate spillover, respectively. Such a behaviour is reminiscent of that of an order parameter in standard order-disorder transitions in statistical physics (see e.g. [37], Ch. 3).

To summarise, numerical exploration of the feasible space of a multi-cellular metabolic system subject

to diffusion-limited lactate exchange suggests that the metabolic activity of cells gives rise to a complex and highly heterogeneous interaction network that couples lactate producers to lactate importers. Environmental lactate accumulation may emerge from imbalances in this network that, depending on the mean oxygen consumption (β_O), can set in abruptly as β_G (i.e. the average net glucose consumption rate) increases. The model is able to reproduce in a stylized way typical bulk overflow-rate curves [7, 12, 38] unraveling the underlying single cell dynamics.

Mean-field theory links the emergent threshold behavior to a phase transition

To further elucidate the behaviour uncovered by sampling \mathcal{F}_N for varying β_G and β_O , we analyzed a mathematically solvable approximation of our constraint-based model. To define it, we focused in particular on the set of constraints (6), which distinguishes \mathcal{F}_N from N independent copies of the single-cell space \mathcal{F}_1 . Upon isolating the contribution of cell i ($i = 1, \dots, N$), the diffusion constraints (6) can be re-cast as

$$u_L^{(i)} + \sum_{j \neq i} A_{ij} u_L^{(j)} \leq 0 \quad (i = 1, 2, \dots, N) \quad (14)$$

The sum on the left-hand-side depends on the specific values of the fluxes $u_L^{(j)}$ as well as on the relative positions of cells (see (7)). For $N \gg 1$, however, it may be well approximated by taking the coefficients A_{ij} to be homogeneous. In particular, we set $A_{ij} = K/N$ for all $i \neq j$, where K is a factor that can be easily estimated for $N \gg 1$ upon neglecting fluctuations. This approximation leads to so-called “fully connected” models in statistical physics [39].

Indeed from

$$\sum_{j \neq i} A_{ij} u_L^{(j)} \simeq K \overline{u_L} \quad , \quad (15)$$

where $\overline{u_L}$ denotes the mean lactate flux across cells, and

$$\sum_{j \neq i} A_{ij} u_L^{(j)} \simeq N \overline{u_L} \frac{R}{d} = \alpha R L \rho \overline{u_L} \quad , \quad (16)$$

with d the mean cell-to-cell distance in a square of size L , $\rho = N/L^2$ the density of cells, and $\alpha \simeq 1.918$ a numerical constant, one finds $K \simeq \alpha R L \rho$ (see Supporting Information, Sec. S1 for the actual numerical values). Within this approximation, we can replace (6) with

$$u_L^{(i)} + K \overline{u_L} \leq 0 \quad (i = 1, 2, \dots, N) \quad (17)$$

Physically, this is equivalent to assuming that the lactate flux of every cell in the population is coupled to a bulk lactate flux to which all cells contribute, known as a ‘mean-field approximation’ in statistical physics (see e.g. [37], Ch. 3).

A detailed examination of the mean-field approximation from this point of view is presented in Supporting Information, Sec. S6, including the analytical solution in the limit $N \rightarrow \infty$. Crucially, in this approximation the constraints (6) become formally identical for all i ’s (see (17)), which effectively reduces the study of the multi-cellular space \mathcal{F}_N to that of the single-cell space \mathcal{F}_1 supplemented with the additional constraint (17). The mean field approximation leads in turn to two non-linear self-consistent equations for two emerging order parameters (see Supporting Information, Sec. S6), one of which can

be identified in the thermodynamic limit with the average net lactate flux, $\langle u_L \rangle$.

Our analytical expression for $\langle u_L \rangle$ is found to define an “overflow curve” that quantitatively reproduces the sampling results of the previous section (see Fig. 3A, compare with Fig. 2C). It turns out that the equations admit an explicit analytical solution as soon as $\langle u_L \rangle < -U_O/(3K)$ while beyond the threshold have to be solved numerically (see Supporting Information, Sec. S6). More precisely, in the regime where the average lactate flux of the population displays threshold-linear behavior, the derivative of $\langle u_L \rangle$ displays a discontinuity at the onset point of overflow metabolism. As displayed in Fig. 3B (top panel), this in turn defines (Supporting Information, Sec. S6) a curve in the (β_O, β_G) plane that separates a phase with large lactate spillover (‘overflow phase’, above the curve) from one without (‘balanced phase’, below the curve). Points along the curve denote critical values of (β_G, β_O) corresponding to the transition between the two regimes. The comparison between numerical simulations and the mean-field analytical predictions shows an excellent quantitative agreement for the flux averages over the whole range of parameters and for the average flux fluctuations ($\sigma_{\overline{u_L}}$) in the unbalanced phase. However, mean-field theory underestimates fluctuations below the phase transition, where the agreement is only qualitative, see Fig. 3A, last panels. This is an expected common pitfall of mean-field approximations across many system and a better characterization of phase transitions in finite dimension would require devoted combinatorial [39] or field-theoretic [37] calculations. One important difference between the two phases is the presence of negative inter-cellular flux correlations in the balanced phase that are absent in the overflow phase where flux fluctuations approximately follow the law of large numbers $\sigma_{\overline{u_L}} \sim \sigma_{u_L}/\sqrt{N}$. Our analytical results therefore provide further quantitative support to the idea that the management of lactate levels in the medium is a genuine emergent phenomenon, achieved through a population-level coordination of lactate exchange fluxes. Likewise, coordination failures triggered by small changes in β_G and/or β_O can lead to excess accumulation of extra-cellular lactate, a characteristic shared with other systems that undergo order-disorder phase transitions.

Inverse modeling experimental data places real cell populations close to criticality

To compare our theoretical scenario with actual experimental data, we focused on recent experiments characterizing the dynamical pH landscape in co-cultures of human pancreatic cancer cells (AsPC-1) and cancer-associated fibroblasts [31]. Advances in nanofibre technology have now made it possible to probe the cellular microenvironment in cultures at high spatial and temporal resolution [40].

In the dataset we considered, local pH data were col-

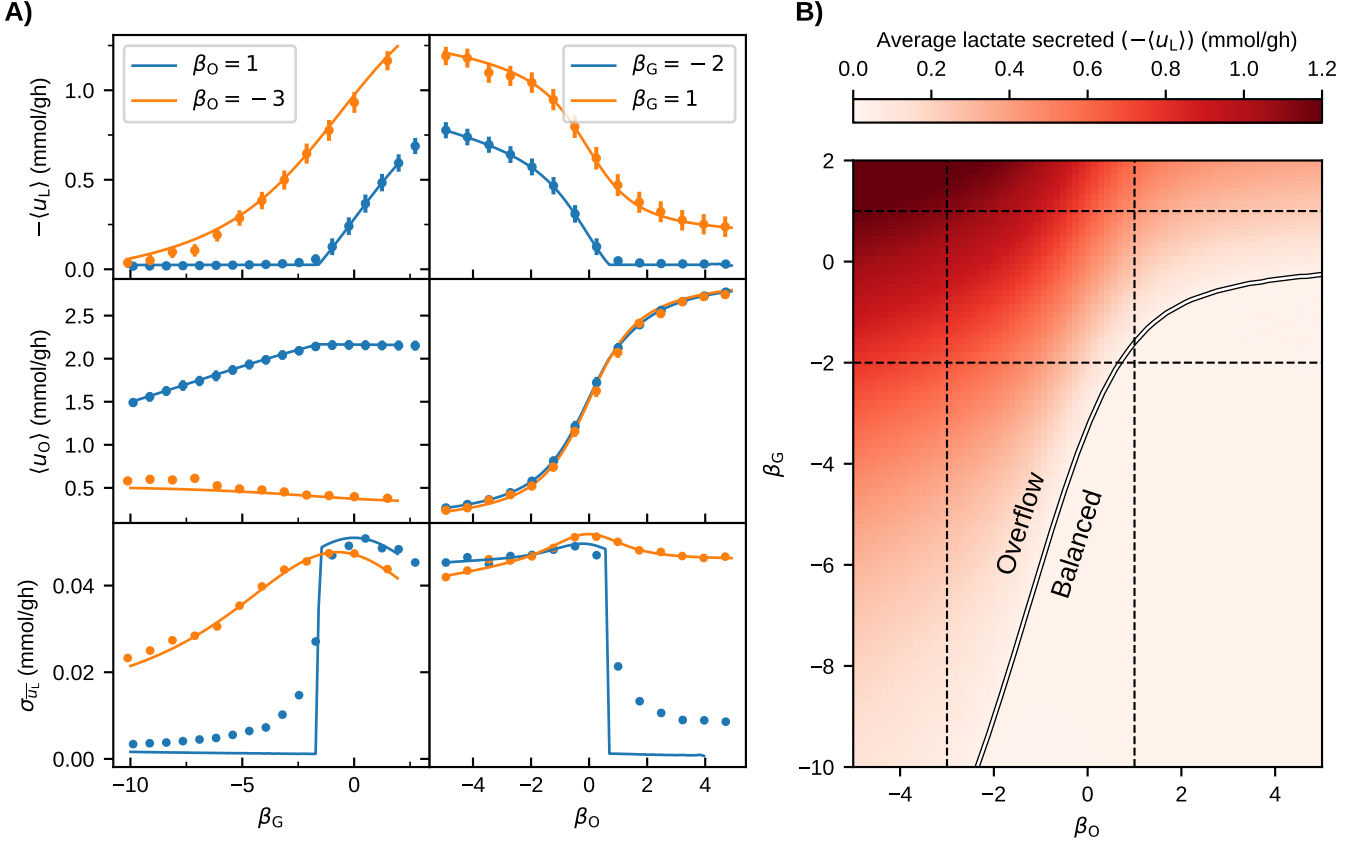


FIG. 3: Mean-field approximation of the CBM simulations. (A) Comparison between mean-field analytics (lines) and numerical simulations (points) for the average lactate flux ($-\langle u_L \rangle$, top), average oxygen flux ($\langle u_O \rangle$, middle), and standard deviation of the average lactate fluxes ($\sigma_{\bar{u}_L}$, bottom) as functions of β_G at fixed β_O (left), and of β_O at fixed β_G (right). Simulations were performed by sampling the feasible space \mathcal{F}_N of $N = 150$ cells spread in an area of $500 \times 500 \mu\text{m}^2$ according to (13) via Hit-and-Run Monte Carlo Markov chains. Analytical lines were obtained by solving the mean-field model (Supporting Information, Sec. S6). (B) Top panel: mean-field phase diagram in the plane spanned by β_O and β_G . The white line is a line of phase transitions where average flux variances are discontinuous (see panel (A)), and separates the ‘overflow phase’ (above the line) from the ‘balanced phase’ (below), the two differing by the rate of lactate accumulation in the medium (background color scale).

lected every 10 minutes over a 6-hour timespan, yielding 36 snapshots of the population’s adaptation (lag phase) to the culture medium. Time-resolved single-cell lactate fluxes for these cultures have been previously obtained by inverse-modeling extracellular proton levels at each time frame (see [31] and Supporting Information, Sec. S7). A highly heterogeneous profile of lactate fluxes was found, which in turn underlies a complex lactate exchange network. We used these data to inform a constrained maximum likelihood inference problem returning the values of β_G and β_O that, at each time frame, yield the best fit of the empirical bulk lactate flux via (13) (Supporting Information, Sec. S8). These are the only two fitted parameters. We then sampled the distributions with the inferred values of β_G and β_O again using Hit-and-Run Monte Carlo, and compared the results against the experimental time course.

Fig. 4A displays a comparison between lactate levels and fluxes from empirical data and simulations over time,

showing for simplicity a reduced set of 6 frames derived by coarse-graining the empirical dataset of 36 snapshots over time by averaging over 6 snapshots (corresponding to about 1 hour) per coarse-grained frame. Besides the qualitative frame-by-frame agreement, one sees how inferred models capture the dynamics of the culture, from an initial state characterized by high environmental lactate levels and strongly heterogeneous single-cell fluxes to a final state with low environmental lactate and reduced flux variability. This point becomes quantitatively clear by comparing empirical distributions of lactate fluxes to theoretical ones (Fig. 4B).

We next mapped the values of (β_O, β_G) that provide the best fits over time onto the phase diagram obtained from the mean-field model (Fig. 4B top). Remarkably, inferred points consistently map around the critical line associated with high inter-cellular exchange and separating the overflow phase from the balanced phase (Fig. 4C). Following a transient, the points display a clear

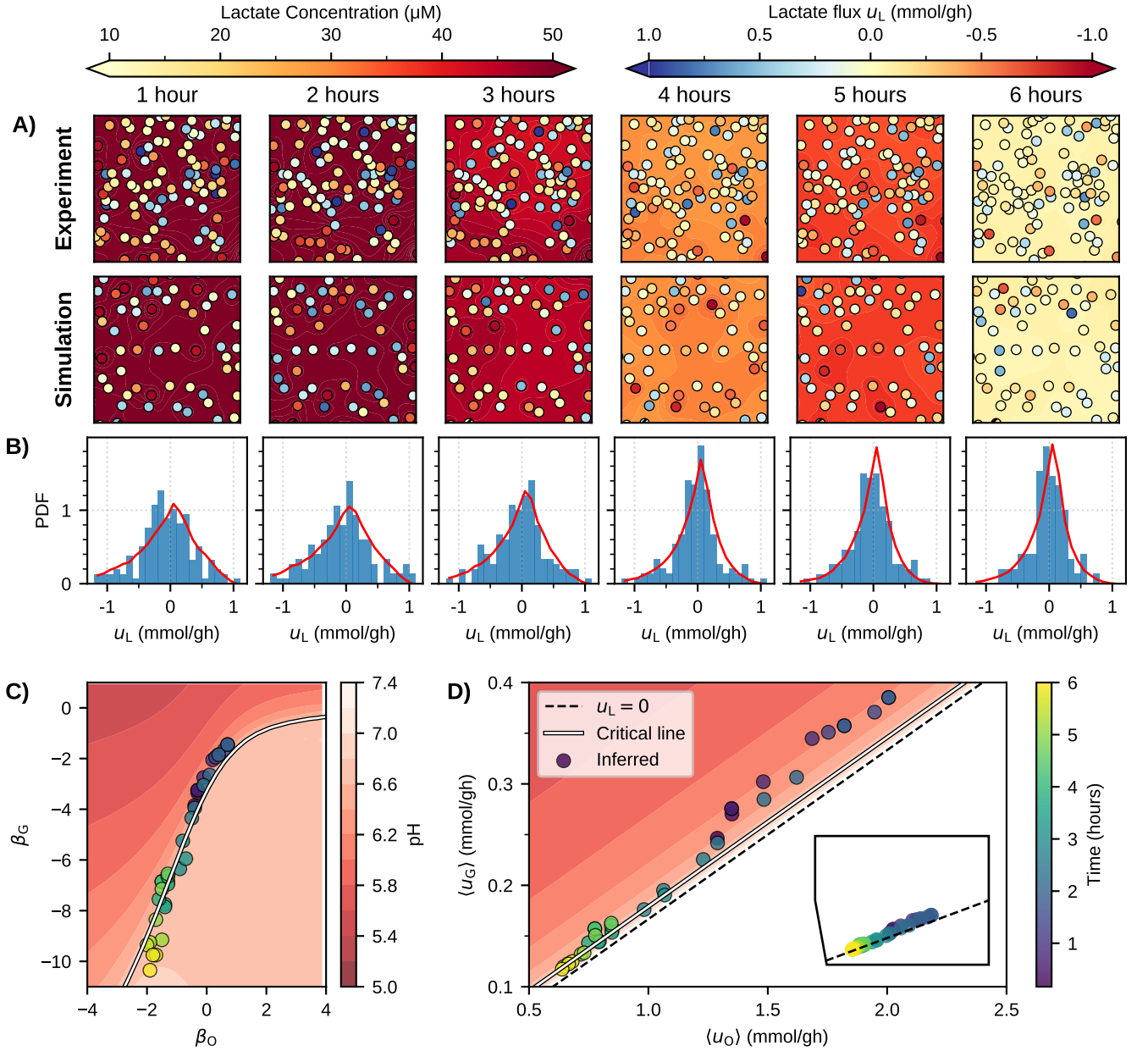


FIG. 4: Comparison between theoretical results and empirical data of Ref. [31]. (A) Snapshots of lactate gradient and single-cell fluxes from coarse grained experimental frames (at intervals of 1h, top) and from CBM simulations performed by sampling (13) with parameters β_G and β_O that, at each time step, provide the maximum likelihood reconstruction of the empirical average lactate flux (bottom). See Supporting Information, for details. (B) Comparison between empirical (bars) and theoretical (lines) single-cell lactate flux distributions at different times for coarse-grained frames. (C) Mean-field phase diagram of Fig. 4B, with the critical line in white, together with inferred values of β_O and β_G (markers) colored according to the time stamp for the 36 frames of the experimental dataset. Estimated contour levels of average pH are provided. (D) Same as (C), but in the plane $(\langle u_O \rangle, \langle u_G \rangle)$. The critical line is again drawn in white. The line corresponding to $\langle u_L \rangle = 0$ is instead blue. (Note that the latter line does not appear in the (β_O, β_G) phase diagram.) Inset: zoomed out view in the single-cell flux space \mathcal{F}_1 of Fig. 1B.

time-ordering that suggests a strong population-level regulation of both β_G and β_O toward negative values. A different representation of the same result is given in Fig. 4D, where the average net glucose and oxygen fluxes ($\langle u_G \rangle$ and $\langle u_O \rangle$, respectively) are used as control param-

eters instead of β_G and β_O . Here one sees that inferred points lie in a region of phase space without deleterious lactate accumulation in the extra-cellular medium with ensuing acidification as it can be seen from the contour levels of the estimated pH in Figs. 4C and D (estimated

from the lactate level Supporting Information, Sec. S7). In short, there is no significant lactate accumulation in the culture in spite of the presence of single cells that sustain large lactate export fluxes (i.e. CO at the level of single cells does not necessarily imply environmental spillover of lactate). Taken together, these results imply that the degree of inter-cellular lactate exchange is coordinated over time to achieve a configuration that lies close to a critical threshold. More specifically, since both the inferred β_G and β_O tend to decrease in time as adaptation to the medium progresses, this population appears to move in the single-cell space \mathcal{F}_1 close to the $u_L = 0$ line and (roughly) toward the state of optimal ATP yield in the balanced regime (see Fig. 4D versus Fig. 1B).

Mitochondrial saturation versus local hypoxia: dynamics of oxygen usage

In light of the above results, it would be important to understand whether, in the observed scenario, lactate production by individual cells is triggered by saturated mitochondrial capacity (which diverts excess carbon towards fermentation) or, rather, by local hypoxic conditions (which limit the oxidative processing of nutrients). In absence of high-resolution data about local oxygen levels in the culture, addressing this question requires an inference framework that goes from learning distributions, to learning single-cell fluxes. To this aim we can use single-cell lactate fluxes derived from the dataset of Ref. [31] along with the estimate for the average oxygen flux derived above to obtain a prediction for single-cell oxidative fluxes via a Boltzmann sampling of the N -cell space of feasible flux configurations \mathcal{F}_N . Theoretical and computational details of the method employed are given in the Supporting Information, Sec. S9. While we are not able to infer unambiguously single cell oxygen fluxes, we can reconstruct a plausible scenario whose key results are given in Fig. 5.

We first notice (Fig. 5A) that, due to a faster diffusion rate, oxygen profiles across the culture appear much more homogeneous than lactate profiles. In addition, single-cell fluxes display a time trend towards downregulation and reduced heterogeneity, a pattern consistent with the time-course of β_O shown in Fig. 4C. This is quantified by how the normalized histogram of single-cell u_O values shifts over time (Fig. 5B). Cells sustaining an oxygen import flux closer to the saturation point ($U_O \sim 2 - 3$ mmol/g/h, see (4)) become more and more rare as time progresses.

A closer look at the time course (Fig. 5C) highlights two distinct regimes in the population's dynamics. The fraction f of saturated mitochondria initially increases as cells seem to increase oxygen consumption (consistently with the transient increase of β_O that is visible in Fig. 4C), leading to a decrease of average environmental oxygen levels c_O . After about 2 hours, f inverts the trend and begins to decrease while c_O concomitantly increases,

signaling that cells have stabilized their metabolism at reduced levels of lactate export, import and exchange (Figs. 4A and B). Note that mitochondrial saturation can occur both under excess glucose intake, leading to the release of lactate in the medium, and under intake of lactate from the medium. We denote by f_- (resp. f_+) the fraction of cells in the former (resp. latter) condition. Fig. 5C shows that, while (perhaps surprisingly) saturation with lactate import is more common, both f_+ and f_- follow the same time trend as f .

Overall, these results, along with evidence that oxygen concentration consistently stays above typical hypoxia levels ($2 - 3$ mg/L of $O_2 \approx 60$ μ mol/L[41]), suggest that the observed dynamics is more likely coupled to the collective behaviour of the population and the emergent exchange network than to a depletion of local environmental oxygen availability.

To further support this idea it is instructive to revisit the phase structure of Figs. 4B and C on the background of the quantities used to analyse oxygen dynamics, reported in detail in Fig. 5D. While macroscopic features appear to be strongly tied to the value of β_O , one notices that the region where acidification is most severe ($\beta_G > 0, \beta_O < 0$) is not generically associated to hypoxic conditions or mitochondrial saturation and, again, both conditions characterize the region where acidification is mild ($\beta_G < 0, \beta_O > 0$). This shows that single-cell and population-level features are separated, the latter being essentially driven by inter-cellular interactions.

DISCUSSION

The broad biological question we faced here asks whether the metabolic phenotype of a multi-cellular system emerges from the interactions among its individual components or is rather the result of a multitude of independent cell-autonomous behaviours. The results we present support the idea that metabolic interactions between cells play a central role in shaping their shared environment, thus influencing the overall fitness of the population. More precisely, cells appear to collectively regulate the levels of medium-acidifying compounds through time-dependent coordination of their exchanges with the surroundings. This process is ultimately sustained by the establishment of cell-to-cell interactions facilitated by the transport of overflow products. In the presence of coordination, environmental spillover is limited despite the presence of cells exporting these compounds at high rates. Conversely, the accumulation of compounds in the medium can be seen as a breakdown of coordination.

Our findings provide robust evidence that the large-scale metabolic organization of cell populations exhibits hallmarks of phase transitions. Therefore, these phenomena can be understood, and possibly controlled, through the application of concepts derived from statistical physics. When viewed through the lens of statistical physics, the transition from a balanced to an unbalanced

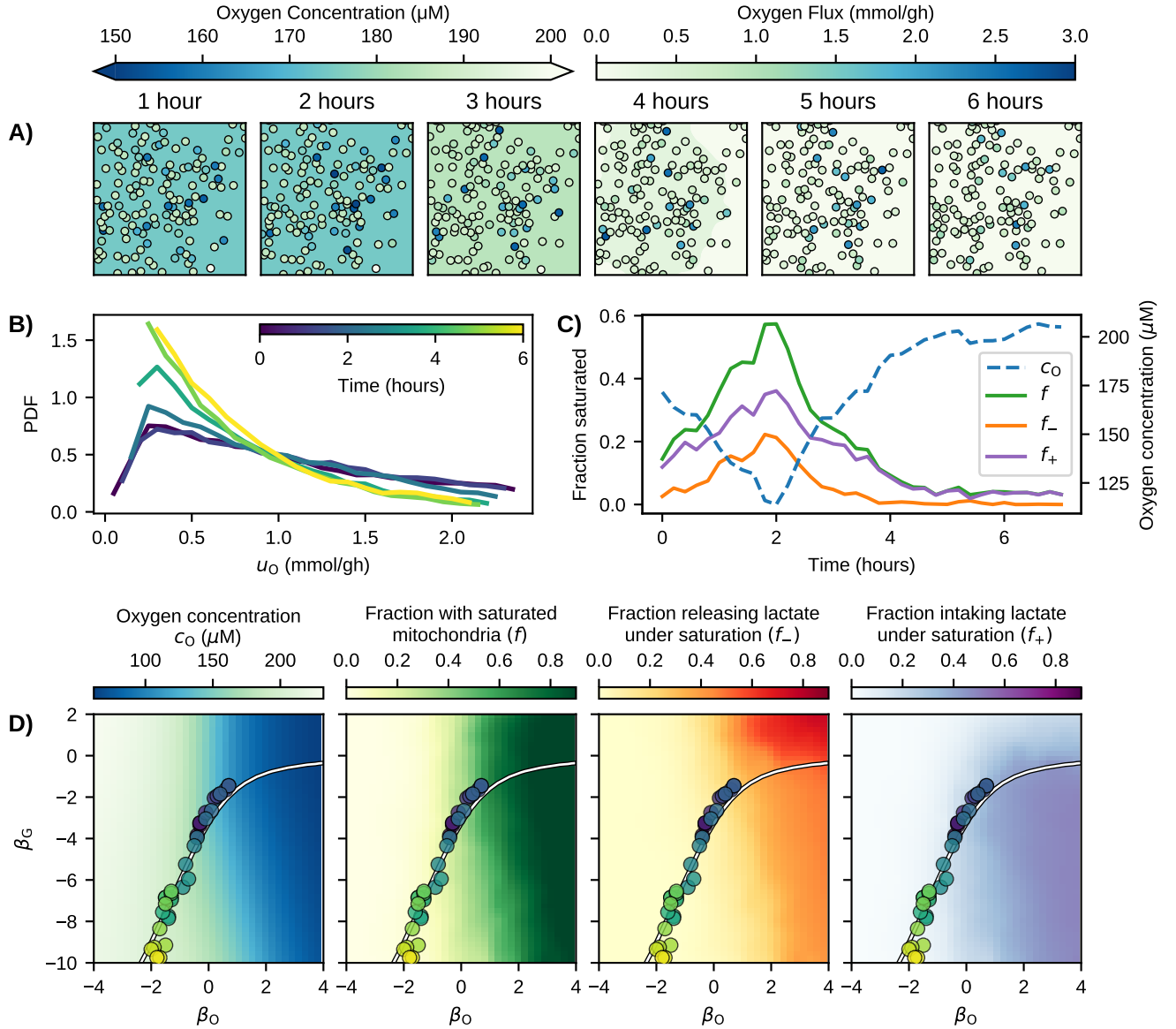


FIG. 5: Inferred dynamics of oxygen usage. (A) Snapshots of oxygen levels and single-cell fluxes inferred from coarse grained experimental frames (at intervals of 1h, top). Note that oxygen fluxes cannot exceed the value $U_O = 3 \text{ mmol/g/h}$ (see (4)). See Supporting Information, Sec. S1 for details. (B) Normalized histogram of inferred single-cell oxygen fluxes at different times from coarse-grained snapshots. (C) Inferred time course for bulk oxygen level (c_O), fraction of cells with saturated oxidative capacity (f), and fraction of saturated cells with lactate release (f_-) and import (f_+). Note: $f = f_- + f_+$. (D) Mean-field phase diagram of Fig. 4B in the (β_O, β_G) plane plotted using the corresponding values of c_O , f , f_- and f_+ as a background heat map. The critical line is in white, while values of β_O and β_G (markers) inferred from the 36 frames of the experimental dataset of [31] are colored according to their time stamp.

state with overflow metabolism bears significant similarities to standard disorder-to-order transitions, e.g. in spin systems. The study of these systems has indeed shown that highly non-trivial macroscopic properties (like phase transitions, symmetry breaking, universality, etc.) can arise from the interaction patterns of large assemblies of simple, identical magnetic spins [30]. In the present case, by using the statistical physics toolbox, we have derived a theoretical ‘critical line’ that separates regimes in the plane spanned by control parameters directly related

to the average glucose and oxygen intakes by the population. Purely theoretical studies of phase transitions and applications of statistical physics methods to ecological settings have been recently put forward [42–44] and our work support this approach providing quantitative empirical evidence on the more basic ground of cellular metabolic dynamics.

On the theoretical side, our research thus confirms that heterogeneous cell populations can be well described by Maximum Entropy distributions like (9) [35, 45–50], sug-

gesting that, at least in some conditions, the constrained maximisation of population-level variability might be a reasonable objective for multi-cellular systems. Moreover, the framework developed here requires inferring only a small number of parameters and constraints (two per time frame) to effectively describe the metabolism of large, spatially organized populations over time. This stands in contrast to the complex task of inverse modeling spiking data using Ising neural networks, which demands inferring thousands of parameters, one for each synaptic connection [51]. Furthermore, an inverse-modeling scheme has shown that experimental data obtained from real cell populations seem to remain close to this critical line as they adapt over time to a given environment. The observation that cultures appear to adapt to a medium by remaining close to a critical line could have important biological implications, since even small changes in the mean import flux of glucose or oxygen, could have drastic effects on cell-to-cell variability and, in turn, on the ability of the population to regulate its environment.

This leaves an important open question, namely why would cell populations tend to remain close to critical in these conditions? In brief, our findings indicate that, by remaining near criticality, a population can curb the environmental costs of carbon overflow while maintaining a large (albeit not maximal) degree of cell-to-cell heterogeneity, for instance in terms of glucose import fluxes, oxygen import fluxes and lactate exchanges. In addition, such a balance appears to be implemented over time, as the population improves the energy yield. The benefits of reducing environmental costs, i.e. pollution of the medium, are self-evident. It is perhaps less clear why a more heterogeneous state (i.e. the critical state) should be preferred to a more homogeneous one (in the balanced phase). A possible explanation lies in the regulatory costs associated to cell-to-cell variability. Among equally fit populations, those with reduced levels of heterogeneity are necessarily subject to tighter regulatory constraints compared to more variable ones, and therefore face larger costs to implement these constraints population-wide [45, 52]. It is therefore reasonable to think that populations that evolve in time to maximise some context-dependent objective function (e.g. growth rate, energy yield, etc.) do so while keeping these regulatory costs as small as possible. In the present case, the performance of the population is affected by two types of costs: one related to lactate spillover, the other due to reduced variability. As the population evolves in time towards an energy-yield optimum, and both β_G and β_O decrease, so does cell-to-cell variability. Critical or near-critical states however appear to consistently strike the optimal balance: above the critical line, environmental costs increase too much; below it, regulatory costs increase too much. All in all, these observations are in line with the idea that ‘critical states’ arising from interactions among their constituents are often crucial to understand the emergence of non-trivial large-scale behaviour

in living systems [53]. Going beyond our case study, implementing this trade-off as a type of programmed cellular behaviour could lead to efficient division of labor within tissues that would confer a selective advantage to multi-cellular organisms.

This scenario admittedly has only been validated using a single dataset and should be contrasted with new evidence coming from single-cell flux data across different experimental conditions (e.g. different cell populations, density, geometry and medium composition). Although recent advancements in high resolution mass-spectrometry hold promise [54, 55], they are currently expensive and invasive. On the other hand, the very recent development of microenvironmental sensing methods [56–59], coupled with ad hoc inverse modeling schemes, could potentially lead to fully time-resolved single-cell metabolic flux analysis.

Besides fundamental aspects, our scenario offers immediate insights in the context of tumor metabolism. In higher organisms, where metabolic behaviour is specialised and compartmentalised according to cell type, the exchange of metabolites such as lactate occurs across multiple scales: organs, tissue and single cells [60]. This division of labour by metabolic specialisation and exchange provides significant benefit to healthy tissue. However, it also renders these systems vulnerable to exploitation by malignant cells, which undergo metabolic rewiring during carcinogenesis [61]. As first observed by Warburg in the 1920s [62], tumours exhibit a notable tendency to consume excessive amounts of glucose while producing lactate, even in the presence of oxygen. However, despite extensive research efforts, a comprehensive understanding of the Warburg effect [63] has remained elusive to date. The approach presented herein supports the idea that the Warburg effect may reflect an emergent feature of a large population of interacting cells characterized by a highly heterogeneous pattern of lactate exchange among individual cells. This would place considerable weight on the ecological dynamics of tumor development, particularly in its early stages. Such a scenario would be fully consistent with recent experimental findings [64].

ACKNOWLEDGMENTS

KN and DDM thank the FBB (Fundación Biofísica Bizkaia) for support. JAPM, RM and ADM acknowledge financial support from the European REA, Marie Skłodowska-Curie Actions, grant agreement no. 101131463 (SIMBAD). DST thanks Biofísica Institute for hosting him while part of this work was carried out. LLDM thanks the Associazione Italiana per la Ricerca contro il Cancro (AIRC) (MFAG-2019, n. 22902) and the PRIN 2022 (2022CRFNCP) funded by the Italian Ministry of Research (MUR) European Union – Next Generation EU.

- [1] Thomas Pfeiffer, Stefan Schuster, and Sebastian Bonhoeffer. Cooperation and Competition in the Evolution of ATP-Producing Pathways. *Science*, 292(5516):504–507, apr 2001.
- [2] Peter Vaupel. Metabolic microenvironment of tumor cells: a key factor in malignant progression. *Experimental oncology*, 32(3):125–7, sep 2010.
- [3] Christian Waltermann and Edda Klipp. Information theory based approaches to cellular signaling. *Biochimica et Biophysica Acta (BBA) - General Subjects*, 1810(10):924–932, oct 2011.
- [4] Aleah F. Caulin and Carlo C. Maley. Peto’s Paradox: Evolution’s prescription for cancer prevention. *Trends in Ecology and Evolution*, 26(4):175–182, 2011.
- [5] Chiara Damiani, Roberto Serra, Marco Villani, SA Kauffman, and A Colacci. Cell–cell interaction and diversity of emergent behaviours. *IET systems biology*, 5(2):137–144, 2011.
- [6] Alan J Wolfe. The acetate switch. *Microbiology and molecular biology reviews*, 69(1):12–50, 2005.
- [7] Alexei Vazquez. *Overflow metabolism: from yeast to marathon runners*. Academic Press, 2017.
- [8] Daan H De Groot, Julia Lischke, Riccardo Muolo, Robert Planqué, Frank J Bruggeman, and Bas Teusink. The common message of constraint-based optimization approaches: overflow metabolism is caused by two growth-limiting constraints. *Cellular and Molecular Life Sciences*, 77:441–453, 2020.
- [9] Yahui Wang, Ethan Stancliffe, Ronald Fowle-Grider, Rencheng Wang, Cheng Wang, Michaela Schwaiger-Haber, Leah P Shriver, and Gary J Patti. Saturation of the mitochondrial nadh shuttles drives aerobic glycolysis in proliferating cells. *Molecular cell*, 82(17):3270–3283, 2022.
- [10] Alexei Vazquez, Qasim K Beg, Marcio A Demenezes, Jason Ernst, Ziv Bar-Joseph, Albert-László Barabási, László G Boros, and Zoltán N. Oltvai. Impact of the solvent capacity constraint on E. coli metabolism. *BMC systems biology*, 2:7, 2008.
- [11] Tomer Shlomi, Tomer Benyamini, Eyal Gottlieb, Roded Sharan, and Eytan Ruppin. Genome-Scale Metabolic Modeling Elucidates the Role of Proliferative Adaptation in Causing the Warburg Effect. *PLoS Computational Biology*, 7(3):e1002018, mar 2011.
- [12] Markus Basan, Sheng Hui, Hiroyuki Okano, Zhongge Zhang, Yang Shen, James R Williamson, and Terence Hwa. Overflow metabolism in escherichia coli results from efficient proteome allocation. *Nature*, 528(7580):99–104, 2015.
- [13] Mariola Szenk, Ken A Dill, and Adam MR de Graff. Why do fast-growing bacteria enter overflow metabolism? testing the membrane real estate hypothesis. *Cell systems*, 5(2):95–104, 2017.
- [14] Matteo Mori, Enzo Marinari, and Andrea De Martino. A yield-cost tradeoff governs escherichia coli’s decision between fermentation and respiration in carbon-limited growth. *NPJ systems biology and applications*, 5(1):16, 2019.
- [15] Yu Chen and Jens Nielsen. Energy metabolism controls phenotypes by protein efficiency and allocation. *Proceedings of the National Academy of Sciences*, 116(35):17592–17597, 2019.
- [16] Matthew G Vander Heiden, Lewis C Cantley, and Craig B Thompson. Understanding the warburg effect: the metabolic requirements of cell proliferation. *science*, 324(5930):1029–1033, 2009.
- [17] Franziska Hirschhaeuser, Ulrike G A Sattler, and Wolfgang Mueller-Klieser. Lactate: A metabolic key player in cancer. *Cancer Research*, 71(22):6921–6925, 2011.
- [18] Alexei Vazquez, Jurre J. Kamphorst, Elke K. Markert, Zachary T. Schug, Saverio Tardito, and Eyal Gottlieb. Cancer metabolism at a glance. *Journal of Cell Science*, 129(18):3367–3373, sep 2016.
- [19] Lucas B. Sullivan, Dan Y. Gui, and Matthew G. Vander Heiden. Altered metabolite levels in cancer: implications for tumour biology and cancer therapy. *Nature Reviews Cancer*, 2016.
- [20] Matthew A Kukurugya and Denis V Titov. The warburg effect is the result of faster atp production by glycolysis than respiration. *bioRxiv*, pages 2022–12, 2022.
- [21] Yihui Shen, Hoang V Dinh, Edward R Cruz, Zihong Chen, Caroline R Bartman, Tianxia Xiao, Catherine M Call, Rolf-Peter Ryseck, Jimmy Pratas, Daniel Weilandt, et al. Mitochondrial atp generation is more proteome efficient than glycolysis. *Nature Chemical Biology*, 2024.
- [22] Karen G de la Cruz-López, Leonardo Josué Castro-Muñoz, Diego O Reyes-Hernández, Alejandro García-Carrancá, and Joaquín Manzo-Merino. Lactate in the regulation of tumor microenvironment and therapeutic approaches. *Frontiers in oncology*, 9:1143, 2019.
- [23] Shayne Mason. Lactate shuttles in neuroenergetics—homeostasis, allostasis and beyond. *Frontiers in neuroscience*, 11:43, 2017.
- [24] Pierre Millard, Sandrine Uttenweiler-Joseph, and Brice Enjalbert. From toxic waste to beneficial nutrient: acetate boosts escherichia coli growth at low glycolytic flux. *bioRxiv*, pages 2022–09, 2022.
- [25] Maria V Liberti and Jason W Locasale. The warburg effect: how does it benefit cancer cells? *Trends in biochemical sciences*, 41(3):211–218, 2016.
- [26] Jorge Fernandez-de Cossio-Diaz, Andrea De Martino, and Roberto Mulet. Microenvironmental cooperation promotes early spread and bistability of a warburg-like phenotype. *Scientific Reports*, 7(1):3103, 2017.
- [27] Xingchen Wang, He Liu, Yingqian Ni, Peibo Shen, and Xiuzhen Han. Lactate shuttle: from substance exchange to regulatory mechanism. *Human Cell*, pages 1–14, 2022.
- [28] Benjamin J Hershey, Sara Barozzi, Fabrizio Orsenigo, Simone Pompei, Fabio Iannelli, Stephan Kamrad, Vittoria Matafora, Federica Pisati, Ludovico Calabrese, Giuseppe Fragale, et al. Clonal cooperation through soluble metabolite exchange facilitates metastatic outgrowth by modulating allee effect. *Science Advances*, 9(37):eadh4184, 2023.
- [29] Aarash Bordbar, Jonathan M Monk, Zachary A King, and Bernhard O Palsson. Constraint-based models predict metabolic and associated cellular functions. *Nature Reviews Genetics*, 15(2):107–120, 2014.
- [30] Hidetoshi Nishimori and Gerardo Ortiz. *Elements of phase transitions and critical phenomena*. Oxford university press, 2011.

- [31] Valentina Onesto, Stefania Forciniti, Francesco Ale-
manno, Krishnadev Narayanankutty, Anil Chandra,
Saumya Prasad, Amalia Azzariti, Giuseppe Gigli, Adri-
ano Barra, Andrea De Martino, et al. Probing single-
cell fermentation fluxes and exchange networks via ph-
sensing hybrid nanofibers. *ACS nano*, 17(4):3313–3323,
2022.
- [32] Jeffrey D Orth, Ines Thiele, and Bernhard Ø Palsson.
What is flux balance analysis? *Nature biotechnology*,
28(3):245–248, 2010.
- [33] Fabrizio Capuani, Daniele De Martino, Enzo Marinari,
and Andrea De Martino. Quantitative constraint-based
computational model of tumor-to-stroma coupling via
lactate shuttle. *Scientific reports*, 5(1):11880, 2015.
- [34] Andrea De Martino and Daniele De Martino. An intro-
duction to the maximum entropy approach and its ap-
plication to inference problems in biology. *Heliyon*, 4(4),
2018.
- [35] Daniele De Martino, Anna Mc Andersson, Tobias
Bergmiller, Călin C Guet, and Gašper Tkačik. Statisti-
cal mechanics for metabolic networks during steady state
growth. *Nature communications*, 9(1):2988, 2018.
- [36] For the filling fraction under exam (below 0.2) a simple
rejection algorithm works to generate the position con-
figurations.
- [37] Giorgio Parisi. Statistical field theory (advanced book
classics). Perseus Pr, 1998.
- [38] Bastian Niebel, Simeon Leupold, and Matthias Heine-
mann. An upper limit on gibbs energy dissipation governs
cellular metabolism. *Nature Metabolism*, 1(1):125–132,
2019.
- [39] Rodney J Baxter. *Exactly solved models in statistical
mechanics*. Elsevier, 2016.
- [40] Ivan Lorenzo Moldero, Anil Chandra, Marta Cavo,
Carlos Mota, Dimitrios Kapsokalyvas, Giuseppe Gigli,
Lorenzo Moroni, and Loretta L Del Mercato. Prob-
ing the ph microenvironment of mesenchymal stromal
cell cultures on additive-manufactured scaffolds. *Small*,
16(34):2002258, 2020.
- [41] Irving P Herman. *Physics of the human body*. Springer,
2016.
- [42] Madhu Advani, Guy Bunin, and Pankaj Mehta. Sta-
tistical physics of community ecology: a cavity solu-
tion to macarthur’s consumer resource model. *Journal
of Statistical Mechanics: Theory and Experiment*,
2018(3):033406, 2018.
- [43] Ada Altieri and Silvio Franz. Constraint satisfaction
mechanisms for marginal stability and criticality in large
ecosystems. *Physical Review E*, 99(1):010401, 2019.
- [44] AR Batista-Tomás, Andrea De Martino, and Roberto
Mulet. Path-integral solution of macarthur’s resource-
competition model for large ecosystems with random
species-resources couplings. *Chaos: An Interdisciplinary
Journal of Nonlinear Science*, 31(10), 2021.
- [45] Daniele De Martino, Fabrizio Capuani, and Andrea
De Martino. Growth against entropy in bacterial
metabolism: the phenotypic trade-off behind empirical
growth rate distributions in e. coli. *Physical biology*,
13(3):036005, 2016.
- [46] Jorge Fernandez-de-Cossio-Diaz , Kalet Leon, and
Roberto Mulet. Characterizing steady states of genome-
scale metabolic networks in continuous cell cultures.
PLoS Computational Biology, 13(11):1–22, 2017.
- [47] Jorge Fernandez-de-Cossio-Diaz and Roberto Mulet.
Maximum entropy and population heterogeneity in con-
tinuous cell cultures. *PLoS Computational Biology*,
15(2):e1006823, 2019.
- [48] Jorge Fernandez-de-Cossio-Diaz and Roberto Mulet.
Statistical mechanics of interacting metabolic networks.
Physical Review E, 123:52–69, 2020.
- [49] David S Tourigny. Dynamic metabolic resource alloca-
tion based on the maximum entropy principle. *Journal
of Mathematical Biology*, 80(7):2395–2430, 2020.
- [50] Marcelo Rivas-Astroza and Raúl Conejeros. Metabolic
flux configuration determination using information en-
tropy. *Plos one*, 15(12):e0243067, 2020.
- [51] Elad Schneidman, Michael J Berry, Ronen Segev, and
William Bialek. Weak pairwise correlations imply
strongly correlated network states in a neural population.
Nature, 440(7087):1007–1012, 2006.
- [52] Anna Paola Muntoni, Alfredo Braunstein, Andrea Pag-
nani, Daniele De Martino, and Andrea De Martino.
Relationship between fitness and heterogeneity in ex-
ponentially growing microbial populations. *Biophysical
Journal*, 121(10):1919–1930, 2022.
- [53] Thierry Mora and William Bialek. Are biological sys-
tems poised at criticality? *Journal of Statistical Physics*,
144:268–302, 2011.
- [54] Lin Wang, Xi Xing, Xianfeng Zeng, S RaElle Jack-
son, Tara TeSlaa, Osama Al-Dalahmah, Laith Z Sama-
rah, Katharine Goodwin, Lifeng Yang, Melanie R
McReynolds, et al. Spatially resolved isotope trac-
ing reveals tissue metabolic activity. *Nature methods*,
19(2):223–230, 2022.
- [55] Luca Rappez, Mira Stadler, Sergio Triana, Rose Muthoni
Gathungu, Katja Ovchinnikova, Prasad Phapale, Math-
ias Heikenwalder, and Theodore Alexandrov. Spacem
reveals metabolic states of single cells. *Nature methods*,
18(7):799–805, 2021.
- [56] Riccardo Rizzo, Valentina Onesto, Giulia Morello,
Helena Iuele, Francesca Scalera, Stefania Forciniti,
Giuseppe Gigli, Alessandro Polini, Francesca Gervaso,
and Loretta L Del Mercato. ph-sensing hybrid hydro-
gels for non-invasive metabolism monitoring in tumor
spheroids. *Materials Today Bio*, 20:100655, 2023.
- [57] Giuliana Grasso, Francesco Colella, Stefania Forciniti,
Valentina Onesto, Helena Iuele, Anna Chiara Siciliano,
Federica Carnevali, Anil Chandra, Giuseppe Gigli, and
Loretta L Del Mercato. Fluorescent nano-and micropar-
ticles for sensing cellular microenvironment: past, present
and future applications. *Nanoscale advances*, 2023.
- [58] Qiang Feng, Zachary Bennett, Anthony Grichuk, Ray-
mundo Pantoja, Tongyi Huang, Brandon Faubert, Gang
Huang, Mingyi Chen, Ralph J DeBerardinis, Baran D
Sumer, et al. Severely polarized extracellular acidity
around tumour cells. *Nature Biomedical Engineering*,
pages 1–13, 2024.
- [59] Giuliana Grasso, Valentina Onesto, Stefania Forciniti,
Eliana D’Amone, Francesco Colella, Lara Pierantoni, Val-
eria Famà, Giuseppe Gigli, Rui L Reis, Joaquim M
Oliveira, et al. Highly sensitive ratiometric fluorescent
fiber matrices for oxygen sensing with micrometer spatial
resolution. *Bio-Design and Manufacturing*, pages 1–15,
2024.
- [60] George A Brooks. Cell-cell and intracellular lactate shut-
tles. *The Journal of physiology*, 587(23):5591–5600, 2009.

- [61] Natalya N Pavlova, Jiajun Zhu, and Craig B Thompson. The hallmarks of cancer metabolism: Still emerging. Cell metabolism, 2022.
- [62] Otto Warburg. The Metabolism of Carcinoma Cells. The Journal of Cancer Research, 9(1):148–163, mar 1925.
- [63] Ralph J DeBerardinis and Navdeep S Chandel. We need to talk about the warburg effect. Nature metabolism, 2(2):127–129, 2020.
- [64] Christopher T Hensley, Brandon Faubert, Qing Yuan, Naama Lev-Cohain, Eunsook Jin, Jiyeon Kim, Lei Jiang, Bookyung Ko, Rachael Skelton, Laurin Loudat, et al. Metabolic heterogeneity in human lung tumors. Cell, 164(4):681–694, 2016.

Supporting Information: Emergent behavior and phase transitions in spatially distributed multi-cellular metabolic networks

K. Narayanankutty, J. A. Pereiro-Morejon, A. Ferrero, V. Onesto, S. Forciniti,
L. L. del Mercato, R. Mulet, A. De Martino, D. S. Tourigny, D. De Martino

Contents

S1 Model parameters and constants	S2
S2 Multi-cellular diffusion constraints	S2
S3 Inter-cellular exchanges and overflow	S3
S4 The partition function	S4
S5 The sampling algorithm	S5
S6 The mean-field approximation	S5
S6.1 Approximation of the partition function	S5
S6.2 Analytical form of $Z(\beta_G, \beta_O, \phi)$ and its derivatives	S7
S6.3 Numerical form of $Z_N(\beta_G, \beta_O)$ and the critical line	S9
S7 The experimental dataset	S10
S7.1 Flux correction due weak acid reversible proton binding	S10
S7.2 Conversion of lactic acid level to pH	S10
S8 Inverse modeling experimental data	S11
S9 Modeling single-cell oxygen dynamics	S12

S1 Model parameters and constants

In Table S1, we provide the actual values of the parameters and constants used with the metabolic network model, including the inter-cellular diffusion constraints.

Name (ID)	Value/range	Unit	Reference
Cell diameter (R)	10	μm	This work
Linear size of culture (L)	1	cm	This work
Number of cells (N)	4×10^4	cells	This work
Mean field constant (K)	40	unit-less	This work**
Average cell dry weight (m)	1	ng	[2]
Maximum molecular oxygen import (U_O)	0.2–0.5	$\text{mmol g}^{-1} \text{h}^{-1}$	[1, 21]
Maximum glucose import (U_G)	0.5	$\text{mmol g}^{-1} \text{h}^{-1}$	[1, 19]
ATP maintenance demand (L_M)	1–10	$\text{mmol g}^{-1} \text{h}^{-1}$	[1, 19]
ATP produced by fermentation	1	ATP per half glucose	[14]
ATP produced by respiration	5	ATP per oxygen (O_2)	[14]
Glucose medium concentrations (c_G)	25	mM	This work
Oxygen medium concentrations (c_O)	0.25	mM	This work
Glucose diffusion constants (D_G)	600	$\mu\text{m}^2 \text{s}^{-1}$	[10]
Oxygen diffusion constants (D_O)	2000	$\mu\text{m}^2 \text{s}^{-1}$	[18]
Lactate diffusion constants (D_L)	1000	$\mu\text{m}^2 \text{s}^{-1}$	[10]
Proton diffusion constants (D_{H^+})	7000	$\mu\text{m}^2 \text{s}^{-1}$	[10]
Oxygen diffusion derived maximum intake (u_O^{\max})	230	$\text{mmol g}^{-1} \text{h}^{-1}$	This work*
Glucose diffusion derived maximum intake (u_G^{\max})	6800	$\text{mmol g}^{-1} \text{h}^{-1}$	This work*

$$(*) u_X^{\max} = 4\pi c_X D_X R/m \quad (**) K = NR/L$$

Table S1: Relevant constants and parameters of the multicellular metabolic network model.

S2 Multi-cellular diffusion constraints

Consider a group of N spherical cells of identical radius R , with centers placed at positions \mathbf{r}_i in a three-dimensional volume V ($i = 1, \dots, N$), such that $|\mathbf{r}_i - \mathbf{r}_j| > 2R$ for any $i \neq j$. We assume that each cell is either a net absorber (flux $u_i > 0$) or a net emitter (flux $u_i < 0$) of a certain compound whose extracellular concentration is represented by a scalar field $c \equiv c(\mathbf{r}, t | \mathbf{r}_c, \mathbf{u})$, where $\mathbf{r}_c = \{\mathbf{r}_i\}$ and $\mathbf{u} = \{u_i\}$. Assuming that no material flow is present in the extracellular fluid and that neither the positions \mathbf{r}_c of cells nor \mathbf{u} change in time, such a field evolves due to (i) cellular emission and absorption, and (ii) random diffusion in V , leading to the diffusive problem

$$\frac{\partial c}{\partial t} = D \nabla^2 c \quad . \quad (1)$$

complemented by suited boundary conditions on the cells surfaces.

We are interested in characterizing its steady state, i.e. the solutions of the *Laplace equation*

$$\nabla^2 c = 0 \quad . \quad (2)$$

Basic mathematical properties like existence and uniqueness of solutions for different classes of boundary conditions are presented in great detail in classical physics textbooks such as [8], Chapters 2 and 3. We focus here on features that are specifically important for the present work.

To begin with, we recall that, for a perfect, isolated spherical absorber with $c = 0$ on the surface and $c = c_\infty$ for $|\mathbf{r}| \equiv r \rightarrow \infty$, the time-dependent diffusion equation (1) is solved by the radial function

$$c(r, t) = c_\infty \left[1 - \frac{R}{r} \left(1 - \text{erf} \frac{r - R}{\sqrt{4Dt}} \right) \right] \quad . \quad (3)$$

Correspondingly, using the diffusion flux $\mathbf{j} = -D \nabla c$, the cellular intake rate is given by

$$u(t) = 4\pi R^2 |j(R, t)| = 4\pi D R c_\infty \left(1 + \frac{R}{\sqrt{\pi D t}} \right) \quad . \quad (4)$$

For $t \rightarrow \infty$ one gets

$$u \rightarrow u_s \equiv 4\pi DRc_\infty \quad \text{and} \quad c \rightarrow c_\infty \left(1 - \frac{R}{r}\right) = c_\infty - \frac{u_s}{4\pi Dr} . \quad (5)$$

(The formula for u_s is known as Smoluchowski's formula.) In the presence of multiple absorbers, shielding effects become relevant and u_s only represents an upper bound to the intake rate of an absorber. Because of the linearity of Laplace's equation, the steady state solution with N absorbers reads

$$c(r) = c_\infty - \sum_i \frac{u_i}{4\pi D|\mathbf{r} - \mathbf{r}_i|} , \quad (6)$$

where u_i represents the uptake flux of cell i . For the sake of stability, at the position of cell j we must have

$$c_\infty \geq \sum_i \frac{u_i}{4\pi D|\mathbf{r}_j - \mathbf{r}_i|} , \quad (7)$$

or, equivalently,

$$u_s \geq \sum_i A_{ji} u_i \quad (\forall j) , \quad (8)$$

where

$$A_{ji} = \delta_{ji} + (1 - \delta_{ji}) \frac{R}{|\mathbf{r}_j - \mathbf{r}_i|} . \quad (9)$$

(We used Kronecker's δ -symbol: $\delta_{ij} = 1$ if $i = j$, and zero otherwise.) Eq. (8) can be seen as a global constraint that diffusion imposes on the feasible values of fluxes u_i . Notice that expression (6) holds in principle also in the presence of emitters with $u_i < 0$. Finally, if there is no reservoir of particles at infinity (i.e. if $c_\infty = 0$), then (8) becomes

$$\sum_i A_{ji} u_i \leq 0 \quad (\forall j) . \quad (10)$$

S3 Inter-cellular exchanges and overflow

Consider a vector $\mathbf{u} = (u_1, \dots, u_N) \in \mathbb{R}^N$ and invertible square matrix $\mathbf{A} \in \mathbb{R}^{N \times N}$. In the main text these are identified with the vector of lactate flux values (i.e. $u_i = -u_L^{(i)}$ is the flux of lactate for the i^{th} cell, note the change in sign) and diffusion constraint matrix \mathbf{A} . Let $\mathbf{1} = (1, \dots, 1)^T$ be the N -dimensional vector of all ones and \mathbf{e}_i be the N -dimensional unit coordinate vector with one in the i^{th} position and zero everywhere else. Then, if we define the extended matrix

$$\mathbf{M} = (\mathbf{A} \quad \mathbf{1} \quad -\mathbf{1}) \quad (11)$$

we have the following equivalence of constraints

$$\mathbf{u}^T \cdot \mathbf{M} \geq 0 \quad \Longleftrightarrow \quad \mathbf{u}^T \cdot \mathbf{A} \geq 0, \quad \mathbf{u}^T \cdot \mathbf{1} = \sum_{i=1}^N u_i = 0. \quad (12)$$

In terms of the main text, this is the statement that a set of lactate flux values satisfies the diffusion constraints with the additional condition that there is no net lactate production. In particular, apart from certain contrived cases, a Flux Balance Analysis optimal yield flux pattern (where all cells are at point **E** in Figure 1B of main text) must have this solution form, since otherwise it would be considered sub-optimal (i.e., there would always be another solution that could obtain a higher value of the objective function by decreasing net lactate production). We now derive a general condition on \mathbf{A} that guarantees the only solution to these constraints is the trivial solution $u_1 = \dots = u_N = 0$.

First note that, for any non-trivial solution \mathbf{u} , there exists some i such that $u_i = \mathbf{u}^T \cdot \mathbf{e}_i < 0$ without loss of generality (since from the constraint $\mathbf{u}^T \cdot \mathbf{1} = 0$ then we must also have some $j \neq i$ with $u_j > 0$). We can therefore write the conditions on a non-trivial solution as

$$\mathbf{u}^T \cdot \mathbf{M} \geq 0, \quad \mathbf{u}^T \cdot \mathbf{e}_i < 0, \quad (13)$$

and from Farkas' Lemma we can have no such \mathbf{u} if we can find a solution to the system of equations

$$\mathbf{M} \cdot \mathbf{y} = \mathbf{e}_i, \quad \mathbf{y} \geq 0. \quad (14)$$

Here $\mathbf{y} \geq 0$ means that all components of \mathbf{y} are non-negative. Explicitly, we have

$$(\mathbf{A} \quad \mathbf{1} \quad -\mathbf{1}) \begin{pmatrix} \mathbf{x} \\ y_2 \\ y_3 \end{pmatrix} = \mathbf{A} \cdot \mathbf{x} + (y_2 - y_3)\mathbf{1} = \mathbf{e}_i, \quad (15)$$

where $\mathbf{x} \geq 0$ and from now on we identify $\lambda \equiv y_2 - y_3 \in \mathbb{R}$. Since \mathbf{A} is invertible, we have

$$\mathbf{x} = \mathbf{A}^{-1} \cdot (\mathbf{e}_i - \lambda \mathbf{1}) \quad (16)$$

and

$$x_j = \mathbf{e}_j^T \cdot \mathbf{x} = (\mathbf{A}^{-1})_{ji} - \lambda \sum_{k=1}^N (\mathbf{A}^{-1})_{jk} \equiv a_{ji} - \lambda B_j \quad (17)$$

where a_{ji} is the $(i, j)^{\text{th}}$ component of the inverse matrix \mathbf{A}^{-1} and B_j is the sum over elements in the j^{th} column of \mathbf{A}^{-1} . Provided B_j is non-zero, from the condition $x_j \geq 0$ for all j we get that we can always find $\lambda \in \mathbb{R}$ whenever

$$\min_{j: B_j > 0} \frac{a_{ji}}{B_j} \geq \max_{j: B_j < 0} \frac{a_{ji}}{B_j}. \quad (18)$$

It therefore follows that, provided this condition on \mathbf{A} is satisfied for all i , then there will be no non-trivial solution to the conditions (12). It can be checked numerically that this condition is satisfied for any sensible choice of inter-cell distance matrix and geometrically corresponds to the intersection of all separating hyper-planes defined by the constraints meeting at just one point. Specifically, this implies that there will be no optimal solution to the maximum yield Flux Balance Analysis problem with lactate exchange between cells.

S4 The partition function

The partition function Z_N for a system of N cells is a function of Lagrange multipliers β_G and β_O given by the following $2N$ -dimensional integral over the multi-cellular flux space \mathcal{F}_N :

$$Z_N(\beta_G, \beta_O) = \int_{\mathcal{F}_N} \prod_{n=1}^N du_G^{(n)} du_O^{(n)} e^{\beta_G u_G^{(n)}} e^{\beta_O u_O^{(n)}}. \quad (19)$$

The partition function also serves as a moment-generating function for the expectation values and higher moments of net fluxes (normalised by the number of cells) defined with respect to the maximum entropy probability measure over multi-cellular flux space. Specifically, given the exponential form of the integrand in (19), we have that

$$\langle u_G \rangle = \frac{1}{N} \frac{\partial}{\partial \beta_G} \ln Z_N(\beta_G, \beta_O) \quad ; \quad \langle u_O \rangle = \frac{1}{N} \frac{\partial}{\partial \beta_O} \ln Z_N(\beta_G, \beta_O), \quad (20)$$

and, by stoichiometry,

$$\langle u_L \rangle = \frac{\langle u_O \rangle}{3} - 2 \langle u_G \rangle. \quad (21)$$

Similarly, variances of these flux values are given by the second-order partial derivatives of Z_N

$$\sigma_{u_G}^2 \equiv \langle u_G^2 \rangle - \langle u_G \rangle^2 = \frac{1}{N^2} \frac{\partial^2}{\partial \beta_G^2} \ln Z_N(\beta_G, \beta_O) \quad ; \quad \sigma_{u_O}^2 \equiv \langle u_O^2 \rangle - \langle u_O \rangle^2 = \frac{1}{N^2} \frac{\partial^2}{\partial \beta_O^2} \ln Z_N(\beta_G, \beta_O). \quad (22)$$

For the variance of the net lactate flux, we use that

$$\langle u_L^2 \rangle = \left\langle \left(\frac{u_O}{3} - 2u_G \right)^2 \right\rangle = \frac{\langle u_O^2 \rangle}{9} + 4 \langle u_G^2 \rangle - \frac{4}{3} \langle u_O u_G \rangle \quad (23)$$

$$\langle u_L \rangle^2 = \left(\frac{\langle u_O \rangle}{3} - 2 \langle u_G \rangle \right)^2 = \frac{\langle u_O \rangle^2}{9} + 4 \langle u_G \rangle^2 - \frac{4}{3} \langle u_O \rangle \langle u_G \rangle \quad (24)$$

which gives

$$\sigma_{u_L}^2 = \left(\frac{\sigma_{u_O}}{3} \right)^2 + (-2\sigma_{u_G})^2 - \frac{4}{3} \text{Corr}[u_O, u_G] \quad (25)$$

where

$$\text{Corr}[u_O, u_G] \equiv \langle u_O u_G \rangle - \langle u_O \rangle \langle u_G \rangle = \frac{1}{N^2} \frac{\partial^2}{\partial \beta_G \partial \beta_O} \ln Z_N(\beta_G, \beta_O). \quad (26)$$

Thus, once $Z_N(\beta_G, \beta_O)$ is known, one can obtain the expectation values and variances of any net flux value as a function of β_G and β_O .

We highlight that, in a more general setting, it is of course possible to introduce $2N$ Lagrange multipliers, one for each cell, that constrain expectation values of each single-cell flux value individually. In that case, the partition function would depend on $2N$ parameters and individual single-cell moments of the flux distribution obtained by differentiation in the same way as described for net flux values above. However, in this work we restrict our focus to a simple, two-parameter model with the goal of parsimoniously reproducing statistical features of existing experimental data and describing the collective behavior of multi-cellular flux distributions. More complex models of the same nature could be applied to experimental data that becomes available in the future.

S5 The sampling algorithm

The multi-cellular metabolic model defines a high-dimensional convex polytope ($D = 2N \approx 300$, where N is the number of cells) and the computational task at hand is to characterize this space, in this case with flux distributions weighted by a Boltzmann factor defined by the maximum entropy constraint. This problem is connected to a class of NP-hard computational problems such as the computation of a matrix permanent, volume of a high-dimensional convex body or the Ising partition function, which can be solved numerically in polynomial time using Markov chain Monte Carlo algorithms [17]. In particular, over-relaxed algorithms like hit-and-run [20] have been shown to work very well in the context of constraint-based genome-scale metabolic modeling, once the ill-conditioning problems connected to heterogeneous scales have been tackled by approximate ellipsoidal rounding [6]. In this work we employed an hit-and-run Markov chain to sample the space, outlined schematically by the following workflow:

0. Initial data: a point P_0 inside the polytope (can be found with a relaxation algorithm such as [12]).
1. Given point P_i , generate a direction/vectors \hat{n} uniformly at random (a point on a unit hyper-sphere, e.g. with the Marsaglia method [11]).
2. Find the intersections t_1, t_2 of the line $L(t) = P_i + t\hat{n}$, $t \in \mathbb{R}$ with the boundary of the polytope.
3. Extract $t^* \in [t_1, t_2]$ by inverting the cumulative distribution function of the marginalized Boltzmann distribution over the segment [11]. Set $P_{i+1} = P_i + t^*\hat{n}$. Return to step 1 (or end the algorithm if you think you have enough points).

It is interesting to notice that, by comparison with the case of sampling steady states of bulk genome scale metabolic networks, the ill-conditioning problem is much less severe in our case. This is due the symmetric structure of the space, which is given by the product of N identical single-cell metabolic flux spaces (plus the diffusion constraints). A code implementation of the sampling algorithm is provided in the repository <https://github.com/KrishnadevN/MulticellularMetabolicNetworks>.

S6 The mean-field approximation

S6.1 Approximation of the partition function

The full partition function (19) can be written explicitly as

$$Z_N(\beta_G, \beta_O) = \int_0^{U_G} \int_0^{U_O} \cdots \int_0^{U_G} \int_0^{U_O} \prod_{n=1}^N du_G^{(n)} du_O^{(n)} e^{\beta_G u_G^{(n)} + \beta_O u_O^{(n)}} \theta(f_{\text{ATP}}^{(n)} - L_M) \theta\left(-u_L^{(n)} - \sum_{\substack{m=1 \\ m \neq n}}^N u_L^{(m)} A_{mn}\right)$$

where we have used the Heaviside step function

$$\theta(x) \equiv \begin{cases} 1, & x \geq 0 \\ 0, & x < 0, \end{cases}$$

to impose the constraints of minimal ATP demand and those given by the diffusion of lactate in the medium. Here, $u_L^{(n)}$ and $f_{\text{ATP}}^{(n)}$ are related to the independent variables $u_G^{(n)}$ and $u_O^{(n)}$ as

$$u_L^{(n)} = \frac{u_O^{(n)}}{3} - 2u_G^{(n)} \quad \text{and} \quad f_{\text{ATP}}^{(n)} = 2u_G^{(n)} + \frac{14}{3}u_O^{(n)}. \quad (27)$$

To obtain an exact expression for Z_N , we make the approximation that $A_{mn} \approx K/N$ for all cells $m \neq n$, which is equivalent to the mean-field approximation that all cells are fully connected and equally distanced, as discussed in the main text. It is important to remark that this approximation also assumes the system to be homogeneous, whereas in general the partition function could depend on the specific spatial positions of individual cells. This homogeneity assumption also means that the moments of the single-cell distribution do not depend on the cell index (n), i.e. the fluxes are identically distributed (albeit correlated) random variables. In particular, when $N \gg 1$ we have

$$\frac{1}{N} \sum_{\substack{m=1 \\ m \neq n}}^N u_L^{(m)} \approx \frac{1}{N} \sum_{m=1}^N u_L^{(m)} \equiv \overline{u_L}, \quad (28)$$

i.e., the contribution of any one cell to the arithmetic mean across cells, $\overline{u_L}$, becomes negligible. With this approximations, the inter-cellular constraint originating from the diffusion of lactate becomes

$$\theta\left(-u_L^{(n)} - \sum_{\substack{m=1 \\ m \neq n}}^N u_L^{(m)} A_{mn}\right) \approx \theta\left(-u_L^{(n)} - K \overline{u_L}\right) \quad (29)$$

so that

$$Z_N(\beta_G, \beta_O) \approx \int_0^{U_G} \int_0^{U_O} \cdots \int_0^{U_G} \int_0^{U_O} \prod_{n=1}^N du_G^{(n)} du_O^{(n)} e^{\beta_G u_G^{(n)} + \beta_O u_O^{(n)}} \theta(f_{\text{ATP}}^{(n)} - L_M) \theta(-u_L^{(n)} - K \overline{u_L}). \quad (30)$$

To manipulate the above integral into a manageable form, we introduce ϕ and λ through the properties of the Dirac delta and its Fourier transform, to express unity as

$$1 = N \int_{-\infty}^{\infty} \delta\left(N\phi - \sum_{n=1}^N u_L^{(n)}\right) d\phi \quad (31)$$

$$= \frac{N}{2\pi} \int_{-\infty}^{\infty} \int_{-\infty}^{\infty} \exp\left(i\lambda \left[N\phi - \sum_{n=1}^N u_L^{(n)}\right]\right) d\phi d\lambda \quad (32)$$

$$= \frac{N}{2\pi} \int_{-\infty}^{\infty} d\phi \int_{-\infty}^{\infty} d\lambda e^{i\lambda N\phi} \prod_{n=1}^N e^{2i\lambda u_G^{(n)} - i\lambda u_O^{(n)}/3}. \quad (33)$$

Inserting this into the integrand of (30), we obtain the identity

$$\prod_{n=1}^N e^{\beta_G u_G^{(n)} + \beta_O u_O^{(n)}} \theta(-u_L^{(n)} - K \overline{u_L}) = \frac{N}{2\pi} \int_{-\infty}^{\infty} d\phi \int_{-\infty}^{\infty} d\lambda e^{i\lambda N\phi} \prod_{n=1}^N e^{(\beta_G + 2i\lambda)u_G^{(n)} + (\beta_O - i\lambda/3)u_O^{(n)}} \theta\left(-u_L^{(n)} - K\phi\right),$$

which enables the approximation of the partition function (30) to be written as

$$Z_N(\beta_G, \beta_O) \approx \frac{N}{2\pi} \int_{-\infty}^{\infty} d\phi \int_{-\infty}^{\infty} d\lambda e^{i\lambda N\phi} [Z(\beta_G + 2i\lambda, \beta_O - i\lambda/3, \phi)]^N \quad (34)$$

$$= \frac{1}{2\pi} \int_{-\infty}^{\infty} d\phi \int_{-\infty}^{\infty} d\lambda \exp[NF(\beta_G, \beta_O, \phi, i\lambda)] \quad (35)$$

with

$$Z(\beta_G, \beta_O, \phi) = \int_0^{U_G} \int_0^{U_O} du_G du_O e^{\beta_G u_G} e^{\beta_O u_O} \theta(f_{\text{ATP}} - L_M) \theta(-u_L - K\phi) \quad (36)$$

and

$$F(\beta_G, \beta_O, \phi, p) = p\phi + \log Z(\beta_G + 2p, \beta_O - p/3, \phi) + \frac{1}{N} \log N. \quad (37)$$

The introduction of ϕ and λ has thus allowed us to “decouple” the diffusion constraints to study the effective two-dimensional, single-cell flux space on which Z is defined.

Finally, to evaluate (35) in the limit $N \rightarrow \infty$, where the $\log(N)/N$ term in (37) can safely be ignored, we use the method of steepest descent (also called the saddle point approximation) [3]. For $N \gg 1$, we obtain

$$\frac{1}{N} \log Z_N(\beta_G, \beta_O) \approx p_* \phi_* + \log Z(\beta_G + 2p_*, \beta_O - p_*/3, \phi_*) \quad (38)$$

where $(\phi_*, p_* \equiv i\lambda^*)$ is the stationary point given by

$$\left. \frac{\partial F}{\partial \phi} \right|_{(\phi_*, p_*)} = 0 \quad \text{and} \quad \left. \frac{\partial F}{\partial p} \right|_{(\phi_*, p_*)} = 0. \quad (39)$$

In particular, from (37), these saddle point equations correspond to the self-consistency equations

$$p^*(\beta_G, \beta_O) = -\frac{\partial}{\partial \phi} \ln Z(\beta_G + 2p_*, \beta_O - p_*/3, \phi_*) \quad (40)$$

$$\phi^*(\beta_G, \beta_O) = -\frac{\partial}{\partial p} \ln Z(\beta_G + 2p_*, \beta_O - p_*/3, \phi_*) \quad (41)$$

where the explicit dependence of p^* and ϕ^* on β_G and β_O is indicated. In fact, by using the chain rule we see that

$$\phi^*(\beta_G, \beta_O) = \left(\frac{1}{3} \frac{\partial}{\partial \beta_O} - 2 \frac{\partial}{\partial \beta_G} \right) \log Z(\beta_G + 2p_*, \beta_O - p_*/3, \phi_*) \equiv \langle\langle u_L \rangle\rangle \quad (42)$$

where $\langle\langle \dots \rangle\rangle$ is the expectation value defined using the measure associated with Z on the effective single-cell space. Namely, from (36) and (42) with $\beta_G^* \equiv \beta_G + 2p^*$ and $\beta_O^* \equiv \beta_O - p^*/3$ we have, self-consistently,

$$\langle\langle \dots \rangle\rangle \equiv \frac{1}{Z(\beta_G^*, \beta_O^*, \langle\langle u_L \rangle\rangle)} \int_0^{U_G} \int_0^{U_O} du_G du_O (\dots) e^{\beta_G^* u_G} e^{\beta_O^* u_O} \theta(f_{\text{ATP}} - L_M) \theta(-u_L - K \langle\langle u_L \rangle\rangle). \quad (43)$$

The values ϕ^* and p^* therefore permit approximation of Z_N using (38) once Z and its derivatives are known. We provide exact analytical formulae for these in the next subsection.

S6.2 Analytical form of $Z(\beta_G, \beta_O, \phi)$ and its derivatives

We now proceed to evaluate the integral defined in (36) to find an analytical formula for $Z(\beta_G, \beta_O, \phi)$ and its derivatives, which are required for computation of the full partition function Z_N . We recall that Z is defined on the effective single-cell space illustrated in Figure S1, restricted to the domain $\phi \leq 0$ due to its evaluation at ϕ^* , as described in the previous subsection. However, we remind the reader that the self-consistent dependence of ϕ^* on β_G and β_O is only imposed after the saddle point approximation so that here ϕ is treated as an independent argument of the three-variable function $Z(\beta_G, \beta_O, \phi)$. The resulting domain of integration can be intuitively thought of as the single-cell flux space from the main text (Figure 1B) combined with an additional upper bound on the rate of lactate uptake, given by the constraint $u_L \leq -K\phi$.

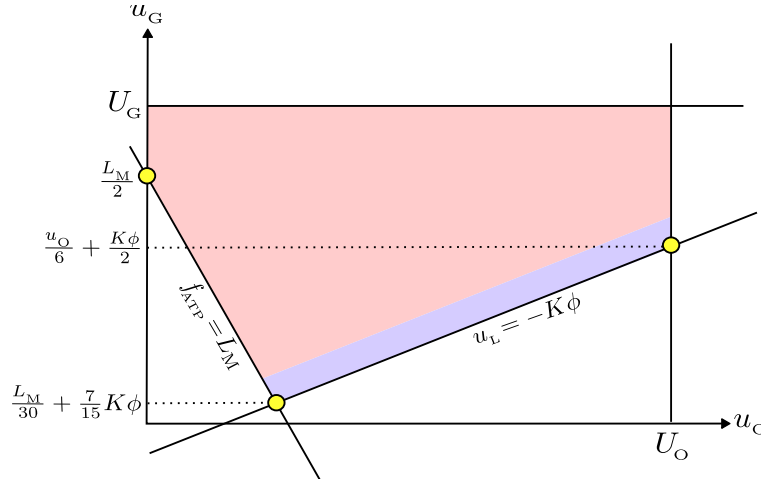


Figure S1: The effective single-cell flux space (in color) given by the limits of integration for $Z(\beta_G, \beta_O, \phi)$. Analogously to the single-cell flux space described in the main text, the pink region has the physical interpretation of lactate export and the purple region denotes lactate import.

In terms of variables u_G, u_O , these constraints give the following limits of integration for the integral in (36):

$$u_G^{\min} \leq u_G \leq U_G \quad ; \quad u_O^{\min} \leq u_O \leq u_O^{\max} \quad (44)$$

where,

$$\begin{aligned}
u_G^{\min} &= \max \left(0, \frac{L_M}{30} + \frac{7}{15} K\phi \right) \\
u_O^{\min} &= \begin{cases} \frac{3}{14} (L_M - 2u_G), & u_G^{\min} \leq u_G \leq u_G^a; \\ 0, & u_G^a \leq u_G \leq U_G \end{cases}; \quad u_G^a \equiv \min \left(\frac{L_M}{2}, U_G \right) \\
u_O^{\max} &= \begin{cases} 6u_G - 3K\phi, & u_G^{\min} \leq u_G \leq u_G^b; \\ U_O, & u_G^b \leq u_G \leq U_G \end{cases}; \quad u_G^b \equiv \max \left(0, \frac{U_O}{6} + \frac{K\phi}{2} \right).
\end{aligned} \tag{45}$$

We evaluate

$$Z(\beta_G, \beta_O, \phi) = \int_{u_G^{\min}}^{U_G} du_G \int_{u_O^{\min}}^{u_O^{\max}} du_O e^{\beta_G u_G} e^{\beta_O u_O} \tag{46}$$

$$= \frac{1}{\beta_O} \int_{u_G^{\min}}^{U_G} du_G e^{\beta_G u_G} e^{\beta_O u_O^{\max}} - \frac{1}{\beta_O} \int_{u_G^{\min}}^{U_G} du_G e^{\beta_G u_G} e^{\beta_O u_O^{\min}}. \tag{47}$$

Since the dependence of u_O^{\min} and u_O^{\max} on u_G changes at u_G^a and u_G^b , respectively, we split each integral into two and obtain

$$\begin{aligned}
Z(\beta_G, \beta_O, \phi) &= \frac{1}{\beta_O} \int_{u_G^{\min}}^{u_G^b} du_G e^{(\beta_G + 6\beta_O)u_G} e^{-3K\phi\beta_O} + \frac{1}{\beta_O} \int_{u_G^b}^{U_G} du_G e^{\beta_G u_G} e^{\beta_O U_O} \\
&\quad - \frac{1}{\beta_O} \int_{u_G^{\min}}^{u_G^a} du_G e^{(\beta_G - \frac{3}{7}\beta_O)u_G} e^{\frac{3}{14}L_M\beta_O} - \frac{1}{\beta_O} \int_{u_G^a}^{U_G} du_G e^{\beta_G u_G}
\end{aligned} \tag{48}$$

which finally gives

$$\begin{aligned}
Z(\beta_G, \beta_O, \phi) &= \frac{e^{-3K\phi\beta_O}}{\beta_O} \left[\frac{e^{\beta_1 u_G^b}}{\beta_1} - \frac{e^{\beta_1 u_G^{\min}}}{\beta_1} \right] + \frac{e^{U_O\beta_O}}{\beta_O} \left[\frac{e^{\beta_G U_G}}{\beta_G} - \frac{e^{\beta_G u_G^b}}{\beta_G} \right] \\
&\quad - \frac{e^{\frac{3}{14}L_M\beta_O}}{\beta_O} \left[\frac{e^{\beta_2 u_G^a}}{\beta_2} - \frac{e^{\beta_2 u_G^{\min}}}{\beta_2} \right] - \frac{1}{\beta_O} \left[\frac{e^{\beta_G U_G}}{\beta_G} - \frac{e^{\beta_G u_G^a}}{\beta_G} \right]
\end{aligned} \tag{49}$$

where

$$\beta_1 \equiv \beta_G + 6\beta_O \quad \text{and} \quad \beta_2 \equiv \beta_G - \frac{3}{7}\beta_O. \tag{50}$$

For evaluating the derivatives, we first note that

$$\frac{\partial}{\partial \beta} \left(\frac{e^{\beta' u}}{\beta'} \right) = \left(u \frac{\partial \beta'}{\partial \beta} + \beta' \frac{\partial u}{\partial \beta} - \frac{1}{\beta'} \frac{\partial \beta'}{\partial \beta} \right) \frac{e^{\beta' v}}{\beta'}. \tag{51}$$

From (50), we have

$$\frac{\partial \beta_1}{\partial \beta_G} = 1 \quad ; \quad \frac{\partial \beta_1}{\partial \beta_O} = 6 \quad ; \quad \frac{\partial \beta_2}{\partial \beta_G} = 1 \quad ; \quad \frac{\partial \beta_2}{\partial \beta_O} = \frac{-3}{7}. \tag{52}$$

For convenience of notation, we also define

$$A = -3K\phi - \frac{1}{\beta_O} - \frac{6}{\beta_1} \quad ; \quad B = \frac{3}{14}L_M - \frac{1}{\beta_O} + \frac{3}{7}\frac{1}{\beta_2}. \tag{53}$$

Using the above, we differentiate (49) term-by-term to obtain

$$\begin{aligned}
\frac{\partial Z}{\partial \beta_G}(\beta_G, \beta_O, \phi) &= \frac{e^{-3K\phi\beta_O}}{\beta_O} \left[\left(u_G^b - \frac{1}{\beta_1} \right) \frac{e^{\beta_1 u_G^b}}{\beta_1} - \left(u_G^{\min} - \frac{1}{\beta_1} \right) \frac{e^{\beta_1 u_G^{\min}}}{\beta_1} \right] \\
&\quad + \frac{e^{U_O\beta_O}}{\beta_O} \left[\left(U_G - \frac{1}{\beta_G} \right) \frac{e^{\beta_G U_G}}{\beta_G} - \left(u_G^b - \frac{1}{\beta_G} \right) \frac{e^{\beta_G u_G^b}}{\beta_G} \right] \\
&\quad - \frac{e^{\frac{3}{14}L_M\beta_O}}{\beta_O} \left[\left(u_G^a - \frac{1}{\beta_2} \right) \frac{e^{\beta_2 u_G^a}}{\beta_2} - \left(u_G^{\min} - \frac{1}{\beta_2} \right) \frac{e^{\beta_2 u_G^{\min}}}{\beta_2} \right] \\
&\quad - \frac{1}{\beta_O} \left[\left(U_G - \frac{1}{\beta_G} \right) \frac{e^{\beta_G U_G}}{\beta_G} - \left(u_G^a - \frac{1}{\beta_G} \right) \frac{e^{\beta_G u_G^a}}{\beta_G} \right]
\end{aligned} \tag{54}$$

and

$$\begin{aligned}
\frac{\partial Z}{\partial \beta_O}(\beta_G, \beta_O, \phi) = & \frac{e^{U_O \beta_O}}{\beta_O} \left(U_O - \frac{1}{\beta_O} \right) \left[\frac{e^{\beta_G U_G}}{\beta_G} - \frac{e^{\beta_G u_G^b}}{\beta_G} \right] + \frac{1}{\beta_O^2} \left[\frac{e^{\beta_G U_G}}{\beta_G} - \frac{e^{\beta_G u_G^a}}{\beta_G} \right] \\
& + \frac{e^{-3K\phi\beta_O}}{\beta_O} \left[\left(A + 6u_G^b \right) \frac{e^{\beta_1 u_G^b}}{\beta_1} - \left(A + 6u_G^{\min} \right) \frac{e^{\beta_1 u_G^{\min}}}{\beta_1} \right] \\
& - \frac{e^{\frac{3}{14} L_M \beta_O}}{\beta_O} \left[\left(B - \frac{3}{7} u_G^a \right) \frac{e^{\beta_2 u_G^a}}{\beta_2} - \left(B - \frac{3}{7} u_G^{\min} \right) \frac{e^{\beta_2 u_G^{\min}}}{\beta_2} \right].
\end{aligned} \tag{55}$$

These analytical formulae form the basis of the self-consistency equations (41) that we solve to obtain Z_N and its derivatives numerically, as described in the next subsection.

S6.3 Numerical form of $Z_N(\beta_G, \beta_O)$ and the critical line

Using the results of the previous two subsections, we are now in a position to calculate Z_N from (38) using ϕ^* and p^* as functions of β_G and β_O , obtained numerically from the self-consistency equations (40) and (41). Python code implementing this procedure is provided in the repository <https://github.com/KrishnadevN/MulticellularMetabolicNetworks>. Importantly, first- and second-order derivatives of Z_N then give the expectation values and variances of net flux values, respectively, as described in Section S4. These are compared with the values obtained from sampling multi-cellular flux space in Figure 3A from the main text. We also confirmed that numerical values for the expectation value of the net fluxes overlap nearly identically with those calculated under the mean-field measure (43), e.g. $\langle u_L \rangle \approx \langle u_L \rangle$, as might be expected in the $N \rightarrow \infty$ limit.

We remark that the analytical form of the self-consistency equations (40) and (41) reveals some important insights into the nature of the phase-transition described by the mean-field model. Inspecting the limits of integration (45), we find a critical value $\phi_c = -U_O/3K$ such that the constraints remain constant for $\phi^* < \phi_c$. Thus, $p^* = 0$ in this region of (β_G, β_O) space, identified with the overflow phase and net lactate production as displayed in Figure S2 and in Figure 3B from the main text. Conversely, in the regime $0 > \phi^* > \phi_c$ the limits of integration become dependent on the value of ϕ^* such that p^* steadily grows as ϕ^* slowly plateaus towards zero. This regime therefore corresponds to the balanced phase with minimal net lactate production. The overall effect is a critical line in phase space that delineates the separation between the balanced and overflow regimes (Figure S2), defined by all critical values (β_G^c, β_O^c) such that $\phi^*(\beta_G^c, \beta_O^c) = \phi_c$. Equivalently, this can be represented as a critical value of $\langle u_L \rangle = -U_O/3K$, as displayed in Figure 4D from the main text.

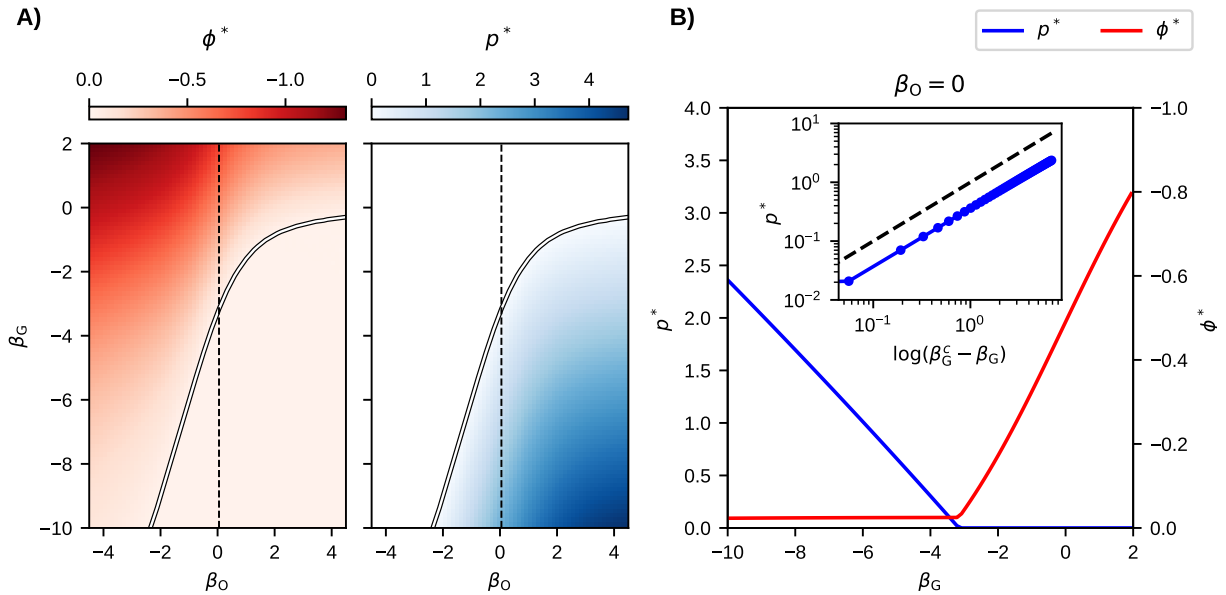


Figure S2: (A) Phase diagrams in the (β_G, β_O) plane: order parameters ϕ^* (left) and p^* (right). The phase diagram is divided by the critical line (continuous white). (B) The order parameters as a function of β_G (for $\beta_O = 0$), corresponding to the dashed line in (A). Inset: p^* as a function of $(\beta_G^c - \beta_G)$ in logarithmic scale showing that the critical exponent is $\alpha = 1$. Here, β_G^c is the critical value of β_G corresponding to $\beta_O = 0$.

S7 The experimental dataset

This work includes experimental data extracted from [15]. Briefly, pH-sensing hybrid nanofibers were fabricated through electrospinning technique starting from polycaprolactone (PCL) polymer dissolved at a concentration of 10% (w/v) in chloroform and dimethyl sulfoxide (DMSO). The PCL solution was mixed with 36 mg mL⁻¹ of ratiometric pH-sensing microparticles based on the pH-indicator dye fluorescein 5(6)-isothiocyanate (FITC) and the reference dye rhodamine B isothiocyanate (RBITC) synthesized as described previously [5]. For cell culture experiments, the pH-sensing nanofibers were placed into a μ -slide 4 well chamber slide with 4×10^4 cells/well of human pancreatic cancer cell line AsPC-1 and cancer-associated fibroblasts (CAFs) in the ratio 70% CAFs and 30% AsPC-1 tumor cells at 37 °C in a humidified 5% CO₂ incubator. The fluorescence response of the pH-sensing nanofibers during cell culture was monitored via time-lapse confocal laser scanning microscopy for 6 hours with a time interval of 10 minutes, maintaining a temperature of 37 °C. Before the experiment, 200 μ L of Leibovitz L15 medium were added to the samples and the calibration of the whole system (pancreatic tumor and pancreatic stromal cells seeded on the pH-sensing nanofibers) was performed. Single-cell fermentation fluxes were inferred by inverse modeling the scalar pH field under the approximation of steady state diffusion from spherical sources and sinks. For further details see [15].

S7.1 Flux correction due weak acid reversible proton binding

Experimental fluxes from the dataset [15] have been re-scaled here by a factor 7, which is approximately the ratio between the diffusion constant of protons and lactate, respectively (see Table S1). The output of experiments in [15] in fact gives more precisely the ratio between the cellular uptake flux and the diffusion constant, the latter assumed to be the one of protons. This assumption, equivalent to a complete dissociation of the acid is incorrect for the case of a weak acid like lactate we are considering here.

S7.2 Conversion of lactic acid level to pH

We will examine the simple case of a uniform dilute solution of acid. The situation can be treated as if the acid HA dissolves first in molecular form and ionises until equilibrium is reached. Let this initial concentration of acid be c . The two contributions to H₃O⁺ in solution are (i) the ionisation of HA and (ii) the self-ionisation of water. Let these concentrations be h_a and h_w respectively. We have,

$$\begin{aligned} [\text{H}_3\text{O}^+] &= [\text{A}^-] + [\text{OH}^-] = h_a + h_w, \\ [\text{HA}] &= c - h_a. \end{aligned}$$

Using the expressions for K_a and K_w , we can write

$$K_a = \frac{[\text{H}_3\text{O}^+][\text{A}^-]}{[\text{HA}]} = \frac{(h_a + h_w)h_a}{c - h_a}, \quad (56)$$

$$K_w = [\text{H}_3\text{O}^+][\text{OH}^-] = (h_a + h_w)h_w. \quad (57)$$

We need to solve the pair of equations for h_a and h_w , given K_a , K_w and c . It is convenient to substitute for $(h_a + h_w)$ and h_w in (57) using (56). Substituting

$$(h_a + h_w) = \frac{K_a(c - h_a)}{h_a} \quad \text{and} \quad h_w = \frac{K_a(c - h_a)}{h_a} - h_a \quad (58)$$

into (57) gives

$$K_w = \frac{K_a(c - h_a)}{h_a} \left[\frac{K_a(c - h_a)}{h_a} - h_a \right], \quad (59)$$

which can be rearranged to get an implicit equation for h_a

$$h_a^2 = \frac{K_a^2(c - h_a)^2}{K_w + K_a(c - h_a)}. \quad (60)$$

This equation can be solved using successive approximations, first assuming $h_a \ll c$, which is valid for a weak acid with low degree of ionisation, to obtain

$$h_a \approx \frac{K_a c}{\sqrt{K_w + K_a c}} \quad (61)$$

and substituting the value back in (60) for an improved estimate. The approximation $c - h_a \approx c$ works best when $c/K_a > 100$ or greater. Further, in the case of lactic acid, $K_a \approx 1.38 \times 10^{-4}$ and $K_w \approx 10^{-14}$ so that, unless the acid solution is very dilute (i.e. if $K_a(c - h_a) \approx K_a c \gg K_w$), (60) can be approximated as

$$h_a^2 \approx K_a(c - h_a) \quad \text{or} \quad h_a \approx \sqrt{K_a c}. \quad (62)$$

To obtain a first approximation of $[\text{H}_3\text{O}^+]$ and hence the pH of the medium, (61) could be substituted in (58) to obtain

$$[\text{H}_3\text{O}^+] = (h_a + h_w) = \frac{K_a c}{h_a} - K_a \approx \sqrt{K_w + K_a c} - K_a. \quad (63)$$

It is to be noted that (58) cannot be used directly when $c \rightarrow 0$, as both the numerator and denominator tend to 0. Instead, when $h_a = 0$, $[\text{H}_3\text{O}^+] = h_w = \sqrt{K_w}$ from (57). It is possible to solve (60) numerically and substitute the value in (58) to obtain $[\text{H}_3\text{O}^+]$ as a function of c .

In our experimental setup, we do not have direct measurements of the concentration of acids. Instead, we have measurements of pH and hence of $[\text{H}_3\text{O}^+]$. So in (56) and (57), the known quantity is $h_a + h_w$ and the unknown is c . We seek an expression for c in terms of $h = h_a + h_w$, given K_a and K_w . We can rewrite (56) and (57) in terms of h and substitute for h_a in (56) using (57) as

$$K_w = h h_w = h(h - h_a) \implies h_a = \left(h - \frac{K_w}{h}\right) \quad (64)$$

$$\begin{aligned} K_a &= \frac{h h_a}{c - h_a} \implies \frac{h}{K_a} = \frac{c}{h_a} - 1 \\ &\implies c = h_a \left(1 + \frac{h}{K_a}\right) \\ &\implies c = \left(h - \frac{K_w}{h}\right) \left(1 + \frac{h}{K_a}\right) \end{aligned} \quad (65)$$

It is easily verified that when $h = h_w = \sqrt{K_w}$, (65) correctly gives $c = 0$. This function $c(h)$ can be numerically inverted to obtain a lookup table for the inverse function $h(c)$, from which we calculate pH as a function of lactate concentration in the medium. We further add an offset term to this formula to match the experimental pH, phenomenologically modeling the buffering of the medium. The resulting conversion curve is shown below in Fig S3.

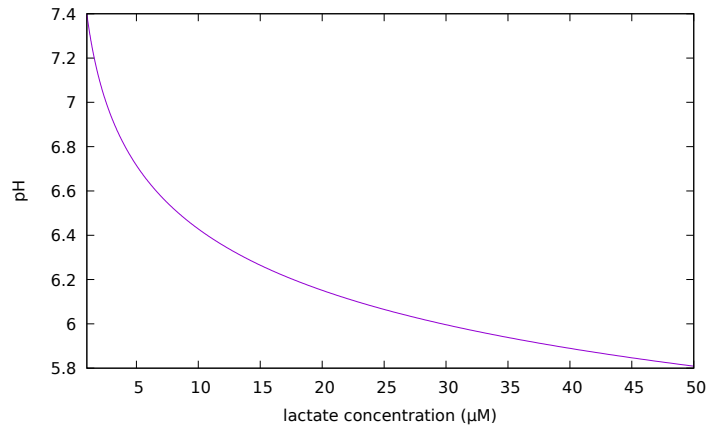


Figure S3: pH as a function of the lactate concentration.

S8 Inverse modeling experimental data

The maximum entropy model we are considering is determined by two parameters, which are the Lagrange multipliers β_G and β_O that fix the average net glucose and oxygen fluxes, respectively, across the cell population. Equivalently, one could consider any other linearly independent combinations of these Lagrange multipliers, such as those fixing the average net fluxes for ATP and lactate production. Ideally, experimental data should therefore provide information about two independent sets of net metabolic fluxes. In this respect, one caveat of

our experimental data is that we have access only to the set of single cell lactate fluxes. However, we can instead exploit the single-cell resolution nature of these data, to fit the first two moments of the observed single-cell experimental lactate flux distribution, which are predicted as functions of β_G and β_O in our model. This leads to a two-parameter predictive model for average net lactate flux and fluctuations (as measured by the standard deviation) that can be fit by minimising the relative error with respect to the experimental values. It turns out that the relative error as a function of the inferred parameters varies little around the critical line leading to a bias towards a critical model. To prevent this, we have considered a prior for β_G and β_O that take into account temporal ordering, i.e. two set of parameters that corresponds to two snapshots of the system at consecutive times are more likely to be similar. This leads to the computational problem of minimising the function

$$E = \sum_t \left[\frac{|\bar{u}_{L,\text{exp}}^t - \langle u_L \rangle_{\text{ME}}(\beta_G^t, \beta_O^t)|}{|\bar{u}_{L,\text{exp}}^t|} + \frac{|\sigma_{L,\text{exp}}^t - \sigma_{L,\text{ME}}(\beta_G^t, \beta_O^t)|}{\sigma_{L,\text{exp}}^t} + \gamma [(\beta_G^t - \beta_G^{t+1})^2 + (\beta_O^t - \beta_O^{t+1})^2] \right] \quad (66)$$

where γ is the regularizer enforcing the temporal prior, and the subscripts exp and ME represent the quantities measured from experiments and those calculated from the model respectively. We have also explicitly indicated the dependence of $\langle u_L \rangle_{\text{ME}}$ and $\sigma_{L,\text{ME}}$ on the parameters β_G^t and β_O^t that we want to infer.

We evaluated $\langle u_L \rangle_{\text{ME}}$ and $\sigma_{L,\text{ME}}$ on a 30×30 grid on the (β_O, β_G) plane, for the rectangle $[-5, 5] \times [-10, 3]$, by performing sampling with the hit-and-run method (see Section S5) and averaging over $P=10^3$ configurations for $N=150$ cells. This provided a lookup table that was further refined by interpolation, which was used to find the set of parameters $\{\beta_G^t, \beta_O^t\}$ that minimize E . The value of γ has been chosen by examining the reconstructed error E as a function of γ , which shows an initial plateau (with average value of 1%) followed by an increase (see fig. S4). We chose the last point of the plateau $\gamma = 0.03$, which corresponds to a strength of the regularizer which restricts the error from increasing in an unconstrained manner.

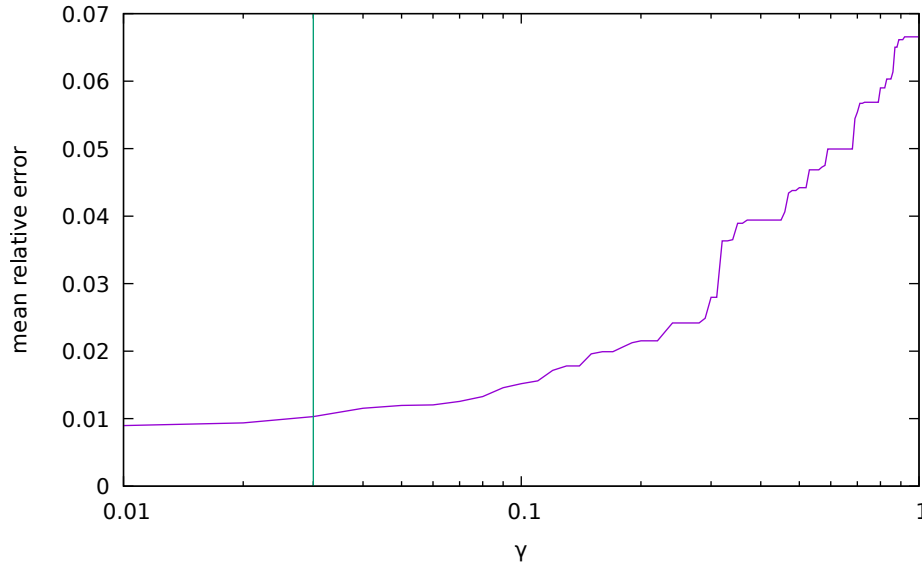


Figure S4: Mean relative error of the fitted experimental data as a function of the prior γ that enforces temporal continuity.

As we remarked in the end of section S4, the setting could be modified beyond the homogeneity assumption and allowing for $2N$ parameters to be inferred. That makes the problem computationally more difficult but still feasible with the help of expectation propagation techniques [4, 13, 16].

S9 Modeling single-cell oxygen dynamics

From the inverse modeling, we have an estimate of the average oxygen flux $\langle u_O \rangle_{\text{ME}}$ that we can complement with the single cell measured value $u_L^{(n)}$ of the lactate flux to obtain single cell estimates of the oxygen fluxes, once again, using the maximum entropy method. The lower bound $\mathcal{L}_O^{(n)}$ and upper bound $\mathcal{U}_O^{(n)}$ for oxygen flux

$u_O^{(n)}$ is calculated using the measured lactate flux $u_L^{(n)}$ as

$$\begin{aligned}\mathcal{L}_O^{(n)} &= \max \left(0, 3 u_L^{(n)}, \frac{M + u_L^{(n)}}{5} \right) \\ \mathcal{U}_O^{(n)} &= \min \left(U_O, 6 U_G + 3 u_L^{(n)} \right).\end{aligned}\tag{67}$$

For cells with $u_L^{(n)} < -2 U_G$, we enforce $u_O^{(n)} = 0$. We then enforce a maximum entropy constraint on the average oxygen flux with a Lagrange multiplier ξ that is independent of the cell index. To obtain the average oxygen flux for the cell n we integrate the marginal Boltzmann probability distribution over the segment $[\mathcal{L}_O^{(n)} \mathcal{U}_O^{(n)}]$

$$\langle u_O^{(n)} \rangle = \frac{\int_{\mathcal{L}_O^{(n)}}^{\mathcal{U}_O^{(n)}} u e^{\xi u} du}{\int_{\mathcal{L}_O^{(n)}}^{\mathcal{U}_O^{(n)}} e^{\xi u} du}\tag{68}$$

that gives

$$\langle u_O^{(n)} \rangle = \frac{\mathcal{U}_O^{(n)} e^{\xi \mathcal{U}_O^{(n)}} - \mathcal{L}_O^{(n)} e^{\xi \mathcal{L}_O^{(n)}}}{e^{\xi \mathcal{U}_O^{(n)}} - e^{\xi \mathcal{L}_O^{(n)}}} - \frac{1}{\xi}.\tag{69}$$

We then match the average $\langle u_O^{(n)} \rangle$ with $\langle u_O \rangle_{\text{ME}}$

$$\frac{1}{N} \sum_{i=1}^N \langle u_O^{(n)} \rangle = \langle u_O \rangle_{\text{ME}}\tag{70}$$

which gives

$$\frac{1}{\xi} = \frac{1}{N} \sum_{n=1}^N \frac{\mathcal{U}_O^{(n)} e^{\xi \mathcal{U}_O^{(n)}} - \mathcal{L}_O^{(n)} e^{\xi \mathcal{L}_O^{(n)}}}{e^{\xi \mathcal{U}_O^{(n)}} - e^{\xi \mathcal{L}_O^{(n)}}} - \langle u_O \rangle_{\text{ME}}\tag{71}$$

The value of ξ obtained solving numerically equation (71) can then be used to estimate $\langle u_O^{(n)} \rangle$ from (69).

This procedure, with our data, does give large errors, i.e. there are many equivalent models with inferred single cell oxygen flux reproducing the lactate data that are compatible with the constraints. Our inferred model can be thus regarded as a “sloppy” one in the sense of [9] and does not lead to real single-cell measurements of the oxygen flux. This is a task that could be finally be achieved with the help of nanometric sensing [7].

References

- [1] Jorge Fernandez-de-Cossio-Diaz, Kalet Leon, and Roberto Mulet. Characterizing steady states of genome-scale metabolic networks in continuous cell cultures. *PLoS Computational Biology*, 13(11):1–22, 2017.
- [2] Makarieva Am, Gorshkov Vg, Li Bl, Chown Sl, Reich Pb, and Gavrilov Vm. Mean mass-specific metabolic rates are strikingly similar across life’s major domains: Evidence for life’s metabolic optimum. *Proceedings of the National Academy of Sciences of the United States of America*, 105(44), 2008.
- [3] Carl M Bender and Steven A Orszag. *Advanced mathematical methods for scientists and engineers I: Asymptotic methods and perturbation theory*. Springer Science & Business Media, 2013.
- [4] Alfredo Braunstein, Anna Paola Muntoni, and Andrea Pagnani. An analytic approximation of the feasible space of metabolic networks. *Nature communications*, 8(1):14915, 2017.
- [5] Anil Chandra, Saumya Prasad, Francesco Alemanno, Maria De Luca, Riccardo Rizzo, Roberta Romano, Giuseppe Gigli, Cecilia Bucci, Adriano Barra, and Loretta L del Mercato. Fully automated computational approach for precisely measuring organelle acidification with optical ph sensors. *ACS Applied Materials & Interfaces*, 14(16):18133–18149, 2022.
- [6] Daniele De Martino, Matteo Mori, and Valerio Parisi. Uniform sampling of steady states in metabolic networks: heterogeneous scales and rounding. *PloS one*, 10(4):e0122670, 2015.
- [7] Giuliana Grasso, Valentina Onesto, Stefania Forciniti, Eliana D’Amone, Francesco Colella, Lara Pierantoni, Valeria Famà, Giuseppe Gigli, Rui L Reis, Joaquim M Oliveira, et al. Highly sensitive ratiometric fluorescent fiber matrices for oxygen sensing with micrometer spatial resolution. *Bio-Design and Manufacturing*, pages 1–15, 2024.

- [8] David J Griffiths. Introduction to Electrodynamics. Cambridge University Press, 2021.
- [9] Ryan N Gutenkunst, Joshua J Waterfall, Fergal P Casey, Kevin S Brown, Christopher R Myers, and James P Sethna. Universally sloppy parameter sensitivities in systems biology models. PLoS computational biology, 3(10):e189, 2007.
- [10] Rudolf Hober, David I. Hitchcock, J. B. Bateman, David R. Goddard, and Wallace O. Fenn. Physical Chemistry of Cells and Tissues. The Journal of Physical Chemistry, 50(4):386–387, 1946.
- [11] Donald E Knuth. The Art of Computer Programming: Seminumerical Algorithms, Volume 2. Addison-Wesley Professional, 2014.
- [12] Werner Krauth and Marc Mézard. Learning algorithms with optimal stability in neural networks. Journal of Physics A: Mathematical and General, 20(11):L745, 1987.
- [13] Anna Paola Muntoni, Alfredo Braunstein, Andrea Pagnani, Daniele De Martino, and Andrea De Martino. Relationship between fitness and heterogeneity in exponentially growing microbial populations. Biophysical Journal, 121(10):1919–1930, 2022.
- [14] David L Nelson, Michael M Cox, and Albert L Lehninger. Lehninger Principles of Biochemistry. W.H. Freeman and Company, 2013.
- [15] Valentina Onesto, Stefania Forciniti, Francesco Alemanno, Krishnadev Narayanankutty, Anil Chandra, Saumya Prasad, Amalia Azzariti, Giuseppe Gigli, Adriano Barra, Andrea De Martino, et al. Probing single-cell fermentation fluxes and exchange networks via ph-sensing hybrid nanofibers. ACS nano, 17(4):3313–3323, 2022.
- [16] José Antonio Pereiro-Morejón, Jorge Fernandez-de Cossio-Diaz, and Roberto Mulet. Inference of metabolic fluxes in nutrient-limited continuous cultures: A maximum entropy approach with the minimum information. Iscience, 25(12), 2022.
- [17] Miklós Simonovits. How to compute the volume in high dimension? Mathematical programming, 97:337–374, 2003.
- [18] W.K. Subczynski and J.S. Hyde. Diffusion of oxygen in water and hydrocarbons using an electron spin resonance spin-label technique. Biophysical Journal, 45(4):743–748, 1984.
- [19] Diana Széliová, Jerneja Štor, Isabella Thiel, Marcus Weinguny, Michael Hanscho, Gabriele Lhota, Nicole Borth, Jürgen Zanghellini, David E. Ruckerbauer, and Isabel Rocha. Inclusion of maintenance energy improves the intracellular flux predictions of CHO. PLOS Computational Biology, 17(6):e1009022, jun 2021.
- [20] VF Turcin. On the computation of multidimensional integrals according to the monte carlo method. Teor. Verojatnost. i Primenen, 16:738–743, 1971.
- [21] Brett A. Wagner, Sujatha Venkataraman, and Garry R. Buettner. The rate of oxygen utilization by cells. Free Radical Biology & Medicine, 51(3):700–712, aug 2011.